A Cenozoic mid-crustal tectonic discontinuity: the Ailao Shan fault, southeastern

Wenkui Fan[1], Junlai Liu[1], Xiaoyu Chen[1], Wei Chen[1], Chunru Hou[1], Baojun Zhou[1], and Hai Nam Dao[1]

[1]China University of Geosciences, Beijing, China

November 22, 2022

Abstract

A crustal section is exposed across the Ailao Shan Tectonic Belt (ALTB) that is suggested to be the accommodation zone of southeastward extrusion of the Sundaland block during the Indian-Eurasian collision. A highly sheared high-grade metamorphic unit (HMU) is separated from the low-grade metamorphic unit (LMU) by an ultramylonite belt, i.e., the previously defined 'Ailao Shan fault'. Rocks in the three units possess identical structural and kinematic characteristics. The ultramylonites exhibit brittle-ductile deformation characteristics in localized middle crustal high strain zone. Geothermometry analyses reveal contrasting deformation P-T conditions across the ultramylonite belt, i.e., 610˜834 , 0.4˜0.6 GPa in the HMU and ca. 400 in the LMU, consistent with microstructural observations and quartz C-axis fabric analysis. The HMU and LMU are kinematically linked while mechanically decoupled, implying shearing of the two units at different crustal levels in the same strain field. Progressive stratified middle to lower crustal flow was responsible for the concurring high- and low-temperature fabrics at different crustal levels. They were juxtaposed during crustal flow in response to extrusion of the Sundaland block at ca. 30˜21 Ma. Exhumation of lower crustal rocks and incision of a thick pile of middle crustal masses were attributed to doming during lower crustal flow. The previously defined 'Ailao Shan fault' occurred as a tectonic discontinuity (TDC) that may have inherited preexisting basement/cover contact along the ALTB. Ubiquitous occurrence of TDCs in middle crust provides a potential explanation for the middle crustal low-velocity and high-conductivity zone beneath the SE Tibet Plateau.

A Cenozoic mid-crustal tectonic discontinuity: the Ailao Shan fault, southeastern Tibetan plateau

Wenkui Fan, Junlai Liu *, Xiaoyu Chen, Wei Chen, Chunru Hou, Baojun Zhou, Hai Nam Dao

State Key Laboratory of Geological Processes and Mineral Resources, China University of Geosciences, Beijing 100083, China

Corresponding author: Junlai Liu (jliu@cugb.edu.cn)

Key points

1. A Cenozoic mid-crustal tectonic discontinuity (TDC) is recognized along previously defined ‘Ailao Shan fault’.
2. Rocks from different crustal levels are juxtaposed along TDC during regional doming associated with stratified middle to lower crustal flow.
3. Ubiquitous occurrence of TDCs provides a potential explanation for the middle crustal LV-HCZ beneath the SE Tibet Plateau.

Abstract

A crustal section is exposed across the Ailao Shan Tectonic Belt (ALTB) that is suggested to be the accommodation zone of southeastward extrusion of the Sundaland block during the Indian-Eurasian collision. A highly sheared high-grade metamorphic unit (HMU) is separated from the low-grade metamorphic unit (LMU) by an ultramylonite belt, i.e., the previously defined 'Ailao Shan fault'. Rocks in the three units possess identical structural and kinematic characteristics. The ultramylonites exhibit brittle-ductile deformation characteristics in localized middle crustal high strain zone. Geothermometry analyses reveal contrasting deformation P-T conditions across the ultramylonite belt, i.e., 610~834 ℃, 0.4~0.6 GPa in the HMU and ca. 400 ℃ in the LMU, consistent with microstructural observations and quartz C-axis fabric analysis. The HMU and LMU are kinematically linked while mechanically decoupled, implying shearing of the two units at different crustal levels in the same strain field. Progressive stratified middle to lower crustal flow was responsible for the concurring high- and low-temperature fabrics at different crustal levels. They were juxtaposed during crustal flow in response to extrusion of the Sundaland block at ca. 30~21 Ma. Exhumation of lower crustal rocks and incision of a thick pile of middle crustal masses were attributed to doming during lower crustal flow. The previously defined 'Ailao Shan fault' occurred as a tectonic discontinuity (TDC) that may have inherited preexisting basement/cover contact along the ALTB. Ubiquitous occurrence of TDCs in middle crust provides a potential explanation for the middle crustal low-velocity and high-conductivity zone beneath the SE Tibet Plateau.

Key words: Ailao Shan fault, tectonic discontinuity, deformation temperatures, kinematic vorticity, crustal incision

1 Introduction

How crustal mass flow in Southeastern Tibet plateau in response to orogenic processes during the Indian-Eurasian continental collision has been a subject of controversy in the last decades (Tapponnier & Molnar, 1976; Tapponnier et al., 1982; Leloup et al., 1995; Royden et al., 1997; Clark & Royden, 2000; Beaumont et al., 2001; Clark et al., 2005; Bai et al., 2010). Tectonic escape model suggests, for

example, that the Sundaland (or Indochina) block extruded southeastward as a rigid block (Tapponnier & Molnar, 1976; Tapponnier et al., 1982). Such a model cannot be applied to explain the present-day GPS measurements that prove a pattern of eastward and southeastward homogeneous flow of upper crustal masses (Wang et al., 2001; Zhang et al., 2004; Gan et al., 2007). Occurrence of exhumed domes in many places may indicate ductile flow of the middle to lower crust in the block interior in late Oligocene to early Miocene (Lacassin et al., 1996; Rhodes et al., 2000; Jolivet et al., 2001; Morley et al., 2002; Wang et al., 2006; Anczkiewicz et al., 2007; Yeh et al., 2008; Xu et al., 2015; Chen et al., 2016, 2017, 2020; Zhang et al., 2017a, b). How rocks from different crustal levels, especially at the middle to lower crustal transition, along a crustal section flow during the continental collision remains poorly understood, although many studies prove the possible existence of the Mattauer (1980) conceptual crustal model in orogenic belts (e.g., Xu et al., 2012; Liu et al., 2018).

The transition of crustal flow deformation pattern is strongly related to structural levels (Fountain & Salisbury, 1981; Carter & Tsenn, 1987; Scholz, 1988). The upper crust is characterized by brittle faulting while the lower crust is dominated by diffuse flow. However, the middle crust is a layer of special geological and geophysical characteristics, e.g., intensive strain-localization (e.g., Simpson et al., 2001), low−velocity and high-conductivity (e.g., Wei et al., 2001). Middle crustal strain-localization generally refers to occurrence of high-strain zones or ductile shear zones (Ramsay, 1980) that are often accompanied by tectonic discontinuities at brittle-ductile conditions in the middle crust (Chen et al., 2016, 2017). As a result of strain weakening at crustal level, the occurrence of strain-localization always couples with decreasing of rock strain strength, high strain accumulation and local increasing of strain rates (Read and Hegemier, 1984), which also contributed to the generation of seismogenic layers in the middle crust (McDonough & Fountain, 1988). Thus, the geometry, kinematics and dynamics of tectonic discontinuity, as well as the P-T conditions for development have been the frontier subjects devoted to the understanding of rheological transition from different structural levels.

The tectonic discontinuity between different structural levels represents a priority

to reconcile crustal equilibrium. The southern Appalachian Mountains (Harris & Milici 1977; Thomas 1990) serve well as typical orogenic thrust system, whereby regional décollement fault, an allochthonous mass of Paleozoic strata displaced over Proterozoic crystalline basement. Décollements enable regional shale mobilization through gravity spreading of their overlying sediment wedges (Evans, 1994). The iconic Whipple Detachment Fault (WDF) on the eastern flank of the Whipple Mountains metamorphic core complex, is the first identified major, low-angle extensional faults separating exposures of rocks from different crustal depths (Yin & Dunn, 1992; Platt & Behr, 2011). The detachment faults were discovered around the globe in the ensuing decades, such as the Hohhot metamorphic core complex, Inner Mongolia, China (Davis et al., 2002) and the Liaonan metamorphic core complex, eastern North China Craton (Liu et al., 2017 and references therein). These distinctive dome-shaped bodies of metamorphic rocks were brought to the surface as the result of extreme extension in Earth's crust. Domal structures that are cored by metamorphic-plutonic rocks, mantled by supracrustal rocks, often of a lower metamorphic grade, and featuring a shear zone draped over the metamorphic core are common in the southeastern Tibetan plateau, corresponding to the development of oblique convergence (e.g., Xuelong Shan complex, Zhang et al., 2017a; Diancang Shan complex, Yan et al., 2021; Yao Shan complex, Chen et al., 2016; Ximeng complex, Chen et al., 2017; Gaoligong complex, Xu et al., 2015; Zhang et al., 2017b).

The Ailao Shan Tectonic Belt (ALTB) occurred as a mobile belt in southeastern Tibetan plateau in response to the Indian-Eurasian collision (e.g. Tapponnier et al., 1990; Schärer et al., 1994; Leloup et al., 1995; Liu et al., 2015 and enclosed references). Intensively sheared high-grade metamorphic rocks of up to granulite facies are well exposed along the main Ailao Shan mountain range. Westward from the main range, there is a transition along crustal section through sheared rocks at greenschist facies to non-metamorphosed rocks. In this context, we present new structural, microstructural, and kinematic vorticity analyses of rock units exposed across the ALTB. Semi-quantitative and quantitative techniques are applied to constrain the transition of deformation-metamorphism condition between the high-

and low-grade metamorphic units. Our strategy is to characterize the internal architecture of the area, and to explore the mechanisms for the occurrence of tectonic discontinuity, which provides a timely opportunity to assess the current understanding of how the lithosphere behaves during collision.

2 **Structural geology of the ALTB**

As one of the most striking lineaments in the southeastern Tibetan Plateau, the ALTB is a major tectonic discontinuity that separates the Yangtze plate from Indochina block. The ALTB extends over 500km in NW-SE direction, from Dali in Yunnan province (China) to Vietnam with a width of ca. 20-30 km and gradually widens to the south (Liu et al., 2012). It is bounded by the Red River fault (RRF) and the Jiujia-Anding fault to the northeast and southwest, respectively. Previous studies revealed that the ALTB is a composite geological boundary that records a long tectonic history from Permo-Triassic Tethyan suturing to Cenozoic extrusion of the Sundaland block (Tapponnier et al., 1990; Leloup, 1995; Zhong, 1998; Liu et al., 2012; Deng et al., 2014). Several rock units and major boundary faults constitute the belt (Figure 1), i.e., the Red River fault (RRF), the high-grade metamorphic unit (HMU), the Ailao Shan fault (ALSF), and the low-grade metamorphic unit (LMU), from east to west across the ALTB (Liu et al., 2012, 2015; Wu et al., 2016, 2017). Further west, Jurassic to Cretaceous rocks gradually transform into the undeformed sedimentary sequence of the Simao-Indosin block (Figure 1).

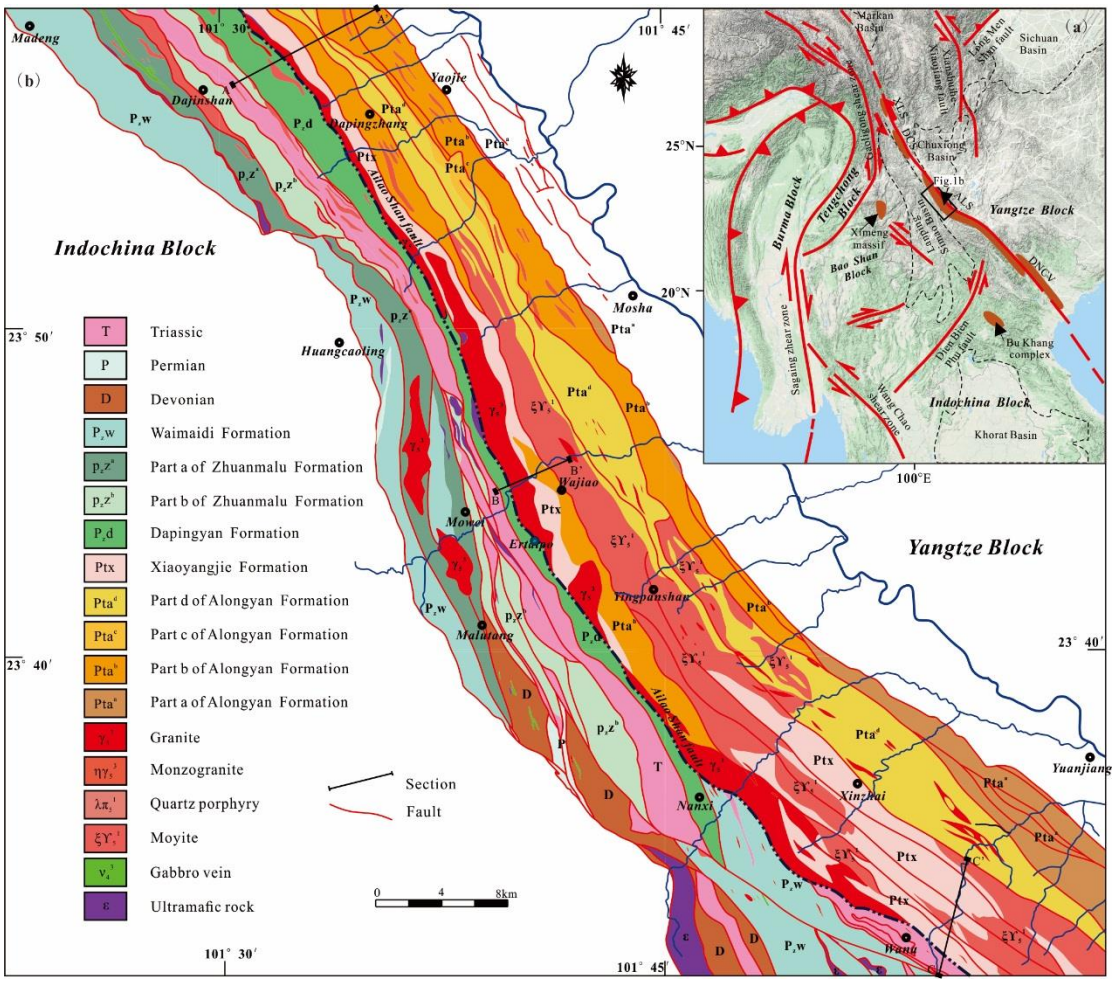

Figure1. (a) Tectonic framework of eastern and southeastern Tibetan Plateau, including major faults systems and microplates in the Sundaland block. XLS– Xuelong Shan; DCS–Diancang Shan; ALS–Ailao Shan; DNCV–Day Nui Con Voi. (b) Detailed structural map of the northern segment of the Ailao Shan Tectonic Belt (modified after BGMRYP, 1990).

The HMU at the northeastern domain consists of interlayered marble, amphibole-plagioclase gneisses, biotite-plagioclase gneisses, two mica-plagioclase gneisses, amphibolites, calc-silicate rocks, quartzite and granitic intrusions of various ages (BGMRYP 1990; Leloup et al., 1995; Tang et al., 2013; Liu et al., 2015). The rocks were highly metamorphosed up to upper amphibolite facies (Leloup et al., 1995; Liu et al., 2012). Migmatitic rocks are ubiquitous and there is local occurrence of granulitic rocks at the southern segment of the ALTB (Leloup & Kienast, 1993; Tran et al., 1998; Gilley et al., 2003; Yeh et al., 2008). One of the most striking features of the HMU is the widespread occurrence of pervasive Cenozoic high-temperature deformation structures in the rocks (Leloup et al., 1995; Liu et al., 2012; Wu et al.,

2017). The LMU to the west of the ALSF consists of a sequence of lower greenschist facies rocks, e.g., phyllites, meta-sandstones and crystallized limestones of Silurian to Cretaceous protoliths (BGMRYP 1990; Leloup et al., 1995; Liu et al., 2012). They were suggested to be derived from Paleozoic shallow-deep water carbonates, clastic rocks and volcanic rocks, of dominantly Paleozoic passive continental margin setting on the western margin of the Yangtze plate (Wu et al., 2016). In contrast to the rocks in the HMU, these rocks are characterized by deformation structures related to low-temperature progressive shearing (Leloup et al., 1995; Liu et al., 2012; Wu et al., 2016).

The ALSF that juxtaposes the HMU and the LMU was suggested to be a boundary of the Ailao Shan shear zone, one of the long-term revival faults with a multi-stage activity history (BGMRYP 1990; Tapponnier et al., 1990; Leloup & Kienast, 1993; Leloup et al., 1995). The fault extends along the west side of the Ailao Shan range and strikes NW-SE. It connected with the Tengtiao River fault southward, while the north segment is cut by the RRF. Previous works defined the fault as the combination of a thrust-nappe and the left-lateral ductile shear zone (Leloup et al., 1995; Zhang et al., 2006). From the following context, it is shown that the ALSF zone is instead a tectonic discontinuity contact that separates two units with linked kinematics but decoupled mechanics.

To the east, the RRF acts as the boundary between the ALTB and the Yangtze block. The fault cuts obliquely across and terminates the northwest end of the Ailao Shan high-grade metamorphic rocks. It continues NW to Erhai Lake to separate Mesozoic red beds of the Lanping-Simao fold belt, showing a component of down-to-the-NE normal displacement (Allen et al., 1984; Leloup et al., 1995; Wang et al., 1998; Replumaz et al., 2001). The RRF is one of the largest active faults in Asia since the Pliocene (Replumaz et al., 2001; Schoenbohm et al., 2006), juxtaposing Triassic to Tertiary red-beds of the Yangtze block directly against high-grade metamorphic rocks along the eastern flank of the ALTB. The Yangtze block consists of Precambrian metamorphic complexes overlain by a thick (>10 km) sequence of late Neoproterozoic (Sinian) to Cenozoic cover rocks (Zhou et al., 2002). The crystalline

rocks include paragneiss, mica schist, graphite-bearing sillimanite–garnet gneiss (khondalite), amphibolite, marble, and quartzite. All of these rocks were tightly folded and experienced local high-grade metamorphism. The cover sequence is composed of clastic, carbonate, and metavolcanic rocks of shallow marine origin. These rocks are weakly metamorphosed to lower greenschist facies, different from the metamorphic rocks of the basement.

3 Structural analysis of the ALTB

3.1 Structural characteristics

Complete profiles of middle to lower crustal rocks are exposed in the ALTB (Leloup et al., 1995; Liu et al., 2012; Wu et al., 2016), where the deformation characteristics of different crustal levels can be approached. From east to west, the following three distinct litho-structural units are recognized according to the deformation characteristics and metamorphic grades, i.e., the high-grade metamorphic unit, an ultramylonite belt, and the low-grade metamorphic unit. Three cross-sections across the northern segment of the ALTB are chosen for detailed structural, microstructural, fabric and thermometric studies of the three units (Figure 2).

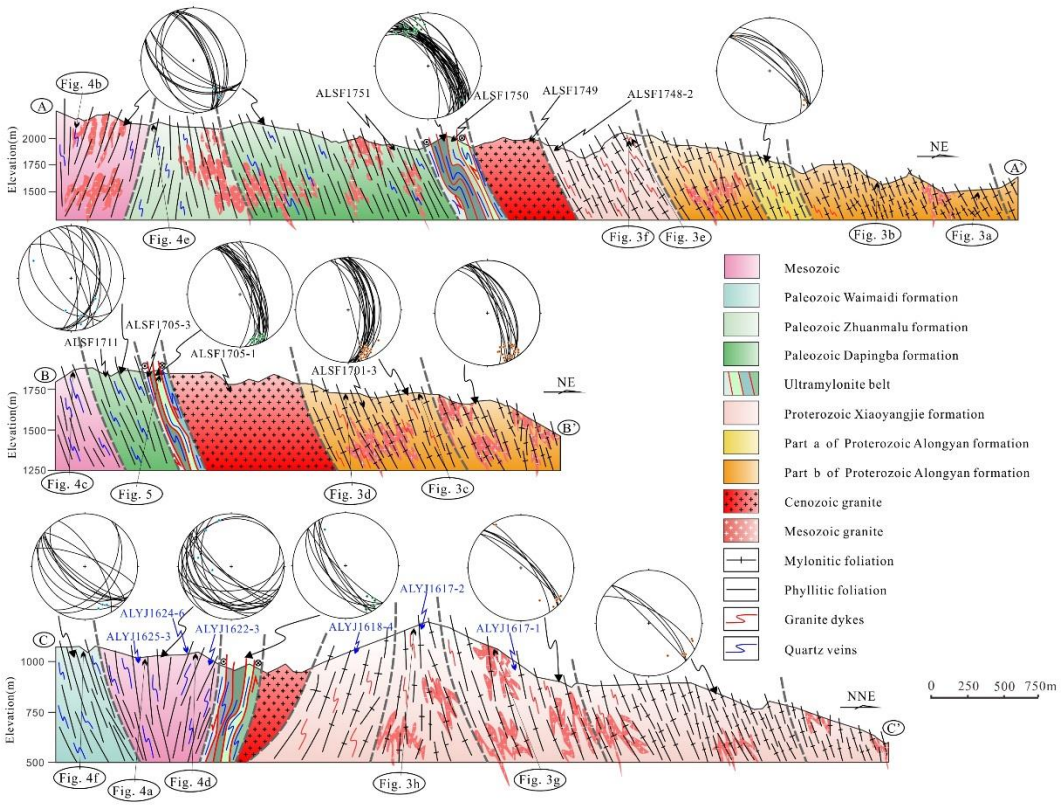

Figure 2. Three cross-profiles from the northern segment of the ALTB (positions in Figure 1b), Stereograms of the foliations (large circle) and stretching lineations (dot) for stations within the northern segment of the ALTB. All diagrams are equal-area Schmidt net, lower hemisphere.

3.1.1 The high-grade metamorphic unit (HMU)

The high-grade metamorphic unit consists of biotite-plagioclase gneisses, amphibolites, two mica schists and polyphase granitic intrusions that have been described as mylonites (Liu et al., 2012; 2015; Wu et al., 2017). These rocks, processed high-grade metamorphism and strong deformation, are characterized by ubiquitous mylonitic foliation (Figure 3a). As in most strongly deformed rocks, the foliation dips to northeast steeply, or to southwest near the ALSF along with profile C (Figure 2). The dip angle ranges from 50° to 80°. The mylonitic foliation (S_1) is marked by the perferred orientation of planar minerals and by flattened quartz or feldspar ribbons. Foliation plane bear prominent NW-SE subhorizontal stretching lineation (Figures 2 and 3b). The plunge angle is lower than 30°. The lineation is defined by elongated biotite streaks, quartz-feldspar rods and by the alignment of metamorphic minerals.

Macroscopic compositional bandings (S_0) consisting of different rocks are generally exhibit elongated symmetrical or asymmetrical tectonic lenses correlating to the locality. Symmetrical lenses with long axis sub-paralleling to the mylonite foliation are abundant, particularly in the orthogneisses of the unit. In contrast, asymmetrical tectonic lenses display effective shear-sense indicators of a top-to-the-southwest thrust shear sense (Figure 3c). A-type folds, with a hinge line parallel to the lineation, are tight to isoclinal and often superpose on the mylonitic bandings (S_{0+1}). The mylonitic foliation is folded around isoclinal folds with NE-dipping axial planes that are parallel to the foliation (Figure 3d). These folds are observed from the outcrop scale and involve passive folding as well as active multilayer buckling. Mylonitic bandings (S_{0+1}) buckling with small-scale parasitic folds occur mostly in and around biotite-rich gneissic layers (Figure 3e). Close to the ALSF, the folds exhibit an increase in asymmetric flanks, suggesting a top-to-the-southwest thrust shear sense. Deformed granitic intrusions are also a part of

the macroscopic banding. Augen granitic mylonites are generally exhibited well-developed foliations and stretching lineations (Figure 3f), a fact suggestive of nearly plane-strain. Various σ- and δ-type porphyroclasts and S-C fabrics (Figure 3g) support an interpretation of left lateral shear. Mylonitic leucogranites display well-developed stretching lineation but rarely-developed foliation (Figure 3h).

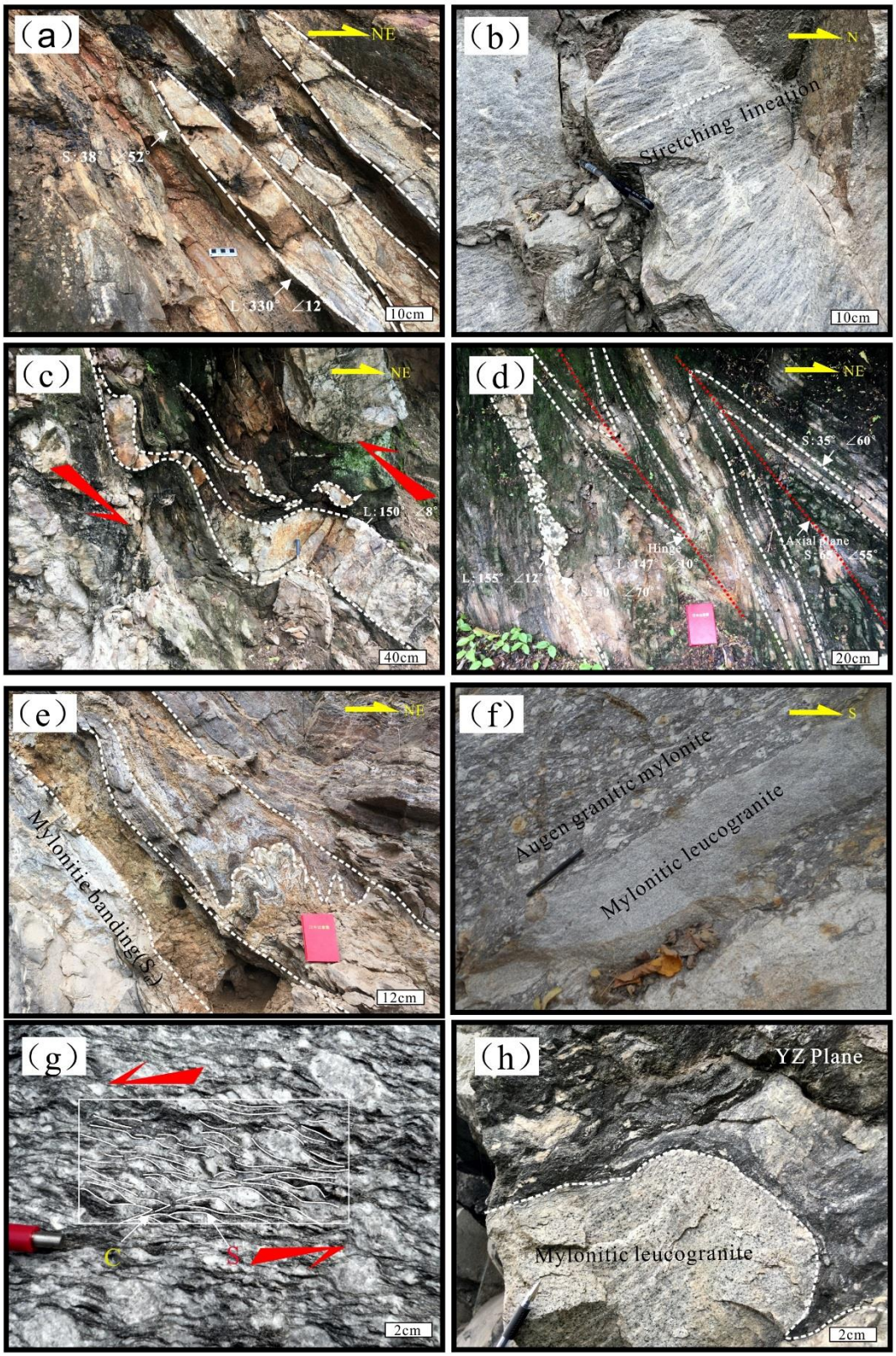

234

235 Figure 3. Outcrops from the high-grade metamorphic unit. (a) Macroscopic compositional
236 bandings experience intensive mylonization, and are characterized by steeply dip foliation. (b)
237 Subhorizontal stretching lineation defined by biotite streaks and quartz-feldspar rods in biotite

schist. (c) Granitic intrusions characterized by asymmetrical folds and tectonic lenses indicate a top-to-the-southwest thrust-sense shearing. (d) Asymmetrical A-type fold with hinge line paralleling to the stretching lineation. (e) Small-scale parasitic folds in the biotite-bearing layers. (f) Multi-stage granitic intrusions exhibit different characteristics in foliation and lineation. (g) S-C fabrics in porphyritic granitic mylonite. (h) Fine-grained mylonitic leucogranite was deformed into L-type tectonite.

3.1.2 The low-grade metamorphic unit (LMU)

The low-grade metamorphic unit consists of Paleozoic metamorphic sandstones, phyllites, and Triassic interbedded limestones, argillaceous and sandy slates, etc. Macroscopic compositional bandings are not obvious. Instead of the original bedding (S_0), the steeply dipping foliation (S_1) and subhorizontal stretching lineation are developed locally in these rocks. It is identical to the gneiss and schists in the high-grade metamorphic unit (Figure 2). The foliation made up of phyllosilicates dips steeply to northeast or southwest in high strain zones but is weakly developed in the lower (Figures 4a and 4b). It shows a dip angle ranging from 43°to 80°. Feldspar and quartz grains are elongated and tend to form in lens-shaped clusters that interbedded between cleavage domains of biotite grains. Besides, elongated micaceous minerals constitute the subhorizontal stretching lineation.

Ubiquitous folds in different types are well-developed, such as horizontal inclined folds and recumbent folds (Figures 4c and 4d), with a tight or broad interlimb angle. These folds were typically folded by pre-existed cleavage/foliation (S_1). Both in the XY plane and the YZ plane, quartz veins in different scales from centimeters to meters were intensively deformed in the form of lenses as well as intestinal or rootless folds (Figures 4e and 4f). The rootless fold is characterized by A-type fold whose hinge line is parallel to the stretching lineation. The rheological contrast between quartz vein and wall rocks leads to fracturing and boudinage of the quartz veins. The fractures apparently represent channels where fluids could enter and further trigger shearing. In some regions, the quartz veins were overprinted, which can be good kinematic indicators for top-to-the-southwest thrust-sense shearing (Figure 4e).

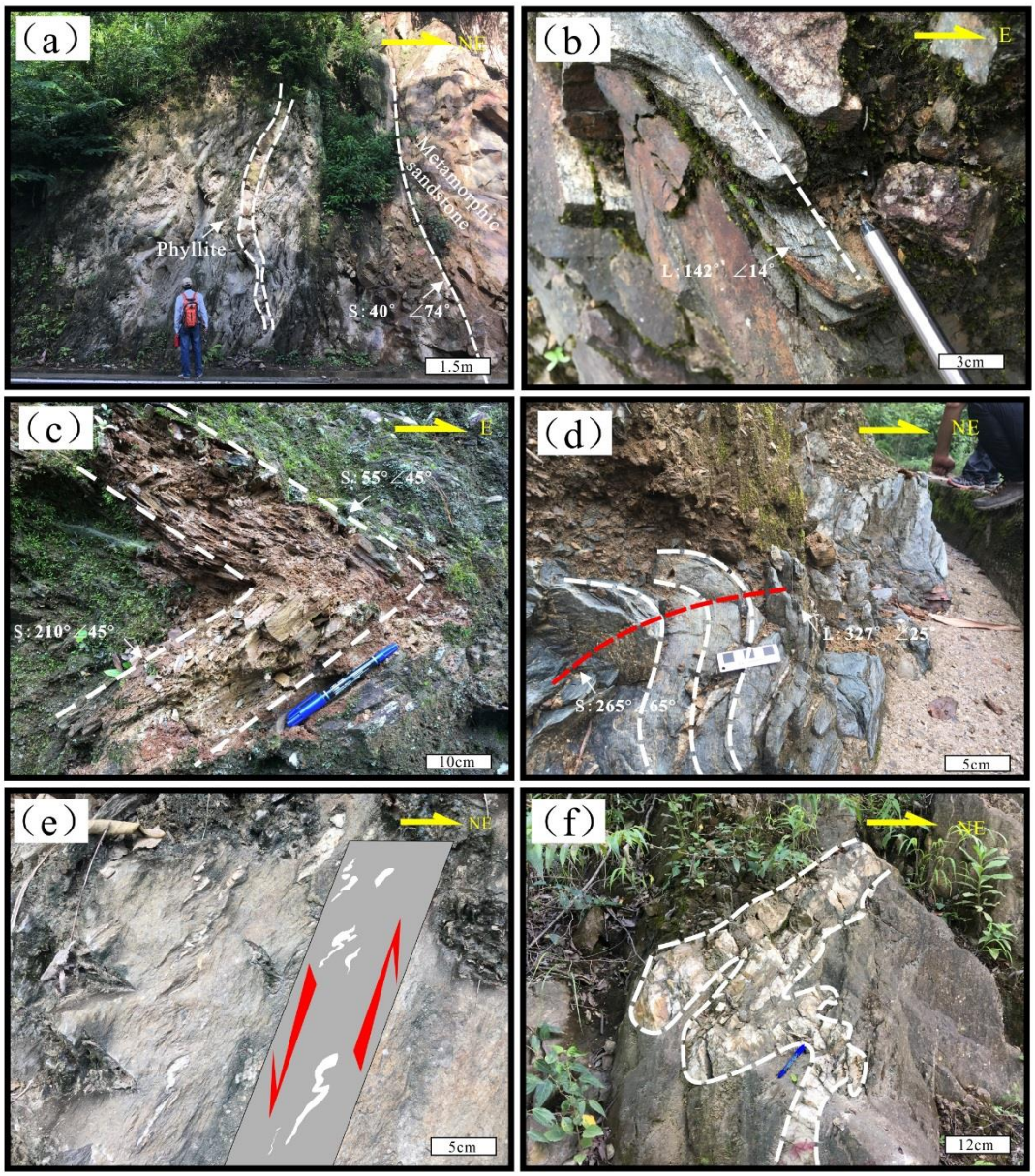

Figure 4. Outcrops from the low-grade metamorphic belt. (a) Alternating distribution of phyllite and metamorphic sandstone with variable dip-angles of foliation. (b) Subhorizontal stretching lineations defined by the orientation of mica aggregates in the phyllite. (c) Recumbent fold resulted from the folding of cleavages in phyllite. (d) Horizontal inclined fold in the crystalline limestone. (e) Rootless folds of quartz veins with kinematic indicators of top-to-the-southwest thrust-sense shearing. (f) Quartz vein in the metamorphic sandstone.

3.1.3 The ultramylonite belt

A narrow NW-SE trending ultramylonite belt consisting of highly foliated phyllonites was observed between the high- and low-grade metamorphic units where

the traditional ALSF is located (Figure 2), however, the elements of brittle fault zone or unconformity have not been found. It behaves as a wavy contact with a width of up to 1000m. To the southwest, it is directly in contact with the Paleozoic to Middle Triassic metasedimentary. To the northeast, it contacts with the Paleoproterozoic paragneiss or schist with high-grade metamorphism higher than upper greenschist facies. Locally, the phyllonites contact with highly deformed granites. Figure 5 explicitly show its relationship between the phyllonites and granites. The latter exhibits a characteristic of L type tectonite with well-developed lineation but rarely-developed foliation. Neoproterozoic and the Early Paleozoic sediments absent within the belt are outcropped along the western margin of the Yangtze block and the southern segment of ALTB. The foliation generally dips to the northeast (e.g., profile A and profile B), but to the southwest locally (e.g., profile C). Stretching lineations defined by fine-grained biotite streaks are preserved on the foliation and plunge to NW or SE sub-horizontally.

At the macroscopic scale, the phyllonite exhibits a texture of alternating stripes. Light-colored stripes are mainly composed of lenticular or elongated feldspar and quartz porphyroclasts, while the dark-stripes have obvious domain structures with fine grains of quartz and biotite filling in the microlithon. Besides, spaced planes separated the phyllonite into slices of different thicknesses (Figure 5b). Quartz veins at different scales distribute sub-parallelly to the foliation and were overprinted into asymmetric folds in some regions, which give perfect kinematic indicators for left-lateral shearing and top-to-the-southwest thrust-sense shearing.

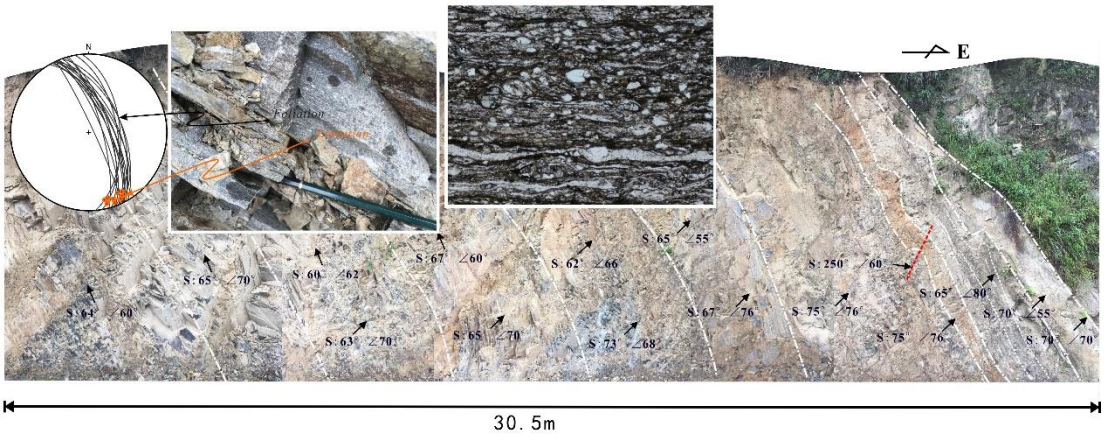

Figure 5. Outcrops and microstructures of rocks from the ultramylonite unit. (a) Outcrop of the ultramylonite unit and the stereograms of the foliation (large circle) and stretching lineation (dot) obtained from phyllonite. (b) Phyllonite exhibits a texture of alternatant-stripes. (c) Minerals with brittle-ductile deformation characteristics in the phyllonite.

3.2 Deformation microstructures and Quartz C-axis LPO fabrics analyses

Deformation microstructures in different rocks are predominantly related to variations in deformation temperatures (e.g., Law et al., 2004, 2013; Liu et al., 2012; Xu et al., 2015; Chen et al., 2016; Zhang et al., 2017b). Within the HMU, high-temperature microstructures of quartz GBM and feldspar SGR are preserved in mylonitic migmatites (Figure 6a). The biotite-plagioclase gneisses show microstructures of rectangular quartz ribbons (Figure 6b). In addition, quartz grains in the mylonitic granites process SGR. BLG and a few myrmekites are developed locally around the feldspar grains (Figure 6c). Larger feldspar porphyroclasts are fractured and filled by quartz veins. Displacement between fragments is consistent with a top-to-the-southwest shearing (Figure 6d). However, in the biotite schist (i.e., ALYJ1617-2) and two-mica schist (i.e., ALYJ1617-1 and ALYJ1618-4) adjacent to the ALSF, that quartz grains share a common optical orientation with vague grain interfaces on account of SGR (Figure 6e). Rounded feldspar grains display BLG, and are overprinted by brittle deformation at lower temperatures. Biotite grains are highly contiguous and grain-size-reduction preserved locally (Figure 6f). New generations of biotite flakes anastomose around quartz grains and are finely intergrown with the flakes of muscovite (Figures 6g and 6h). These microstructures indicate the schists were deformed at a high temperature (550-700 ℃, Passchier & Trouw, 2005; Law, 2014). In contrast, metamorphic sandstone (i.e., ALYJ1622-3) in the LMU preserves its original matrix-support texture, where quartz grains are elongated with long-axis orientation, showing conspicuous undulatory extinction and weak BLG (Figures 6m and 6n). In the phyllites (i.e., ALYJ1624-6 and ALYJ1625-3), quartz grains exhibit BLG and undulatory extinction while feldspar grains present brittle micro-fractures (Figure 6o). These microstructures may be consistent with the dominant deformation at low temperature (300-400 ℃, Passchier & Trouw, 2005; Law, 2014). It is

noteworthy that the foliation (S1) of fine-grain micas and the original bedding (S0) in phyllite make it looks like S-C tectonite (Figure 6p). Decoupling to the HMU and LMU, phyllonite in the ultramylonite belt is composed of fine-grained quartz, feldspar, and sericite (Figure 6i). Quartz grains show BLG, while feldspar grains exhibit obvious brittle fractures and are replaced by sericite locally (Figure 6j). These microstructures imply that dominant deformation in the phyllonite is under low temperature (350-400 ℃, Passchier & Trouw, 2005; Law, 2014). Locally, the quartz grains show weakly-developed SGR (Figures 6j and 6l). It probably represents a pro-stage relatively high-temperature deformation.

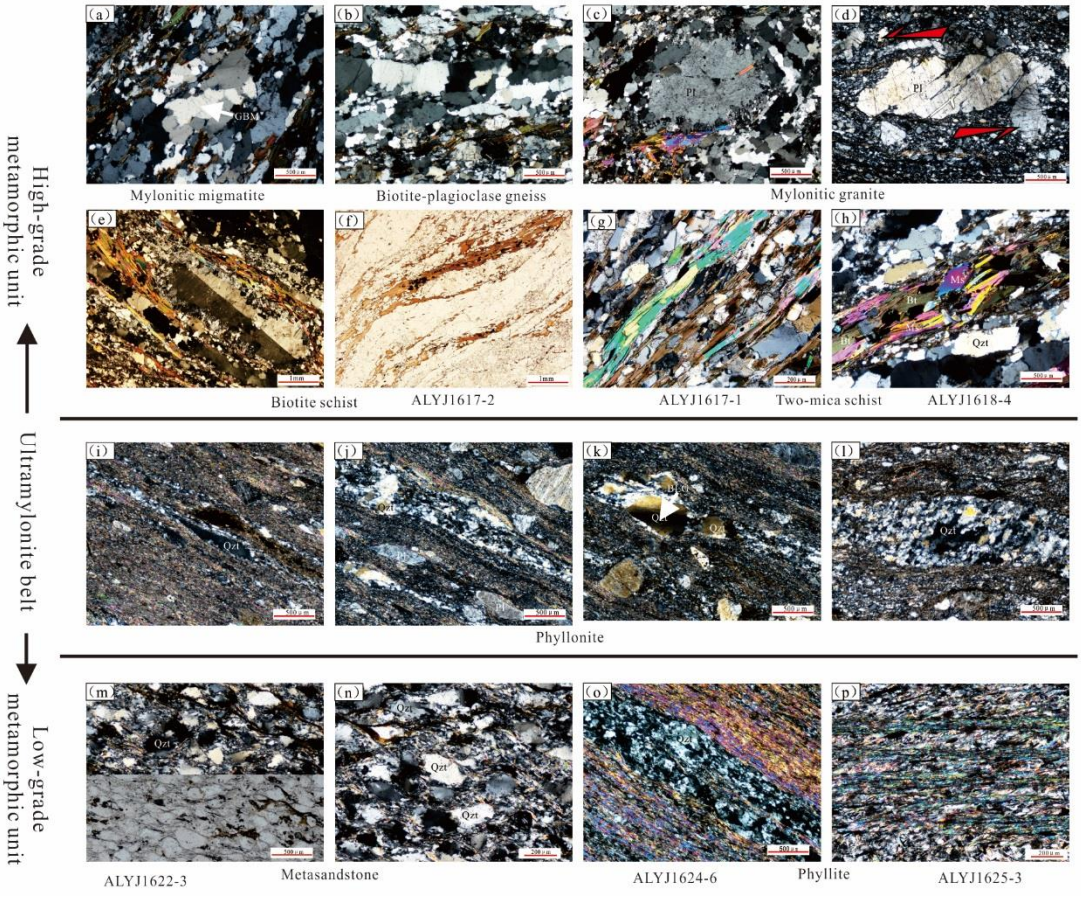

Figure 6. Microstructures of rocks from the HMU, ultramylonite belt, and the LMU. (a) Microstructures in the mylonitic migmatite of quartz GBM and feldspar SGR. (b) The rectangular quartz ribbons in the biotite-plagioclase. (c) The mylonitic granite is characterized by quartz SGR and feldspar BLG and myrmekites. (d) The fractured feldspar porphyroclast in the YZ plane shows a kinematic indictor of top-to-the-southwest shearing. (e) Upper greenschist facies biotite schist showing quartz SGR and feldspar BLG. (f) The microstructures of contiguous biotite and

grain size reduction in biotite schist. (g)-(h) The prominent foliation defined by oriented biotites and muscovites in the two mica schists. The quartz SGR and feldspar BLG is ubiquitous. (i)-(l) The microstructures of phyllonites in the ultramylonite. The phyllonite is composed of matrix and prophyroclast. The latter if featured by quartz BLG and undulatory extinction and feldspar fracturing. (m)-(n) The metasandstone is characterized by quartz BLG and undulatory extinction where the original matrix-support texture is preserved. (o) Quartz vein in the phyllite shows a characteristic of quartz BLG and undulatory extinction. (p) Cleavage (S1) and original bedding (S0) in the phyllite constitute the S-C tectonite.

The quartz C-axis analyses are approached by EBSD to determine the dominant slip system, and further to determine the deformation temperature (Passchier & Trouw, 2005; Trouw et al., 2010). Quartz C-axis fabric analyses (Table 1) indicate that the deformation temperature is consistent well with deformation microstructures but entirely individual at the HMU and the LMU. In the HMU, quartz LPO patterns of biotite schist (i.e., ALYJ1617-2) and two-mica schist (i.e., ALYJ1617-1 and ALYJ1618-4) are strongly characterized by a point maxima near or at the periphery of the Y-axis, which can be referred to as type I crossed girdles or sub-maxima near the Z-axis locally (Figures 7a-7c, Schmid & Casey, 1986), indicating that quartz experienced multi-stage deformation and is controlled by different slip systems. It was dominated by prism <a> slip for dislocation creep under medium- to high-temperature (550-650 ℃) at an early stage. However, crossed girdles or sub-maxima here is related to the basal <a> slip and rhomb <a> slip for medium- to low-temperature deformation (400-500 ℃) superimposition at the late stage, which weakly contributed to the quartz C-axis fabrics (Schmid & Casey, 1986; Stipp et al., 2002). On the contrary, quartz LPO patterns in the LMU, typically the metasandstone (i.e., ALYJ1622-3) and phyllite (i.e., ALYJ1624-6 and ALYJ1625-3) adjacent to the ALSF, is characterized by low temperature. The quartz type I crossed girdles and a relatively weak sub-maxima can be found at the periphery of the Z-axis (Figures 7d-7f). These fabrics suggest a complicated quartz LPO pattern of a combination of rhomb <a> slip at relatively low temperature (350-450 ℃) and basal <a> slip at low temperature (<350 ℃) (Schmid & Casey, 1986; Stipp et al., 2002). The pattern of deformation

overprinting in the LMU is consistent and comparable with that in the HMU.

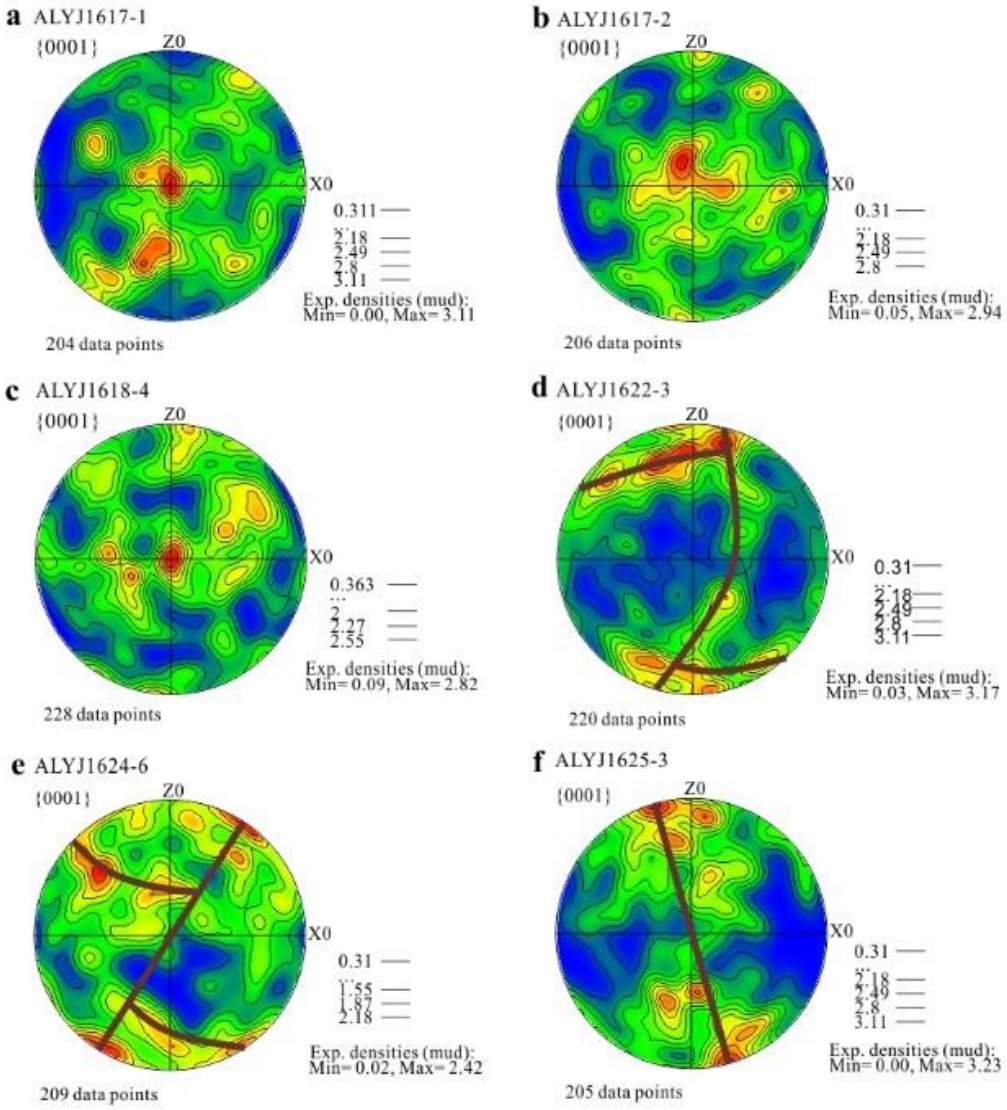

Figure 7. Quartz C-axis fabrics of samples collected from the northern segment of the ALTB. The contours at multiples of a uniform distribution are plotted. Structural directions: X0–parallel to the lineation, Z0–normal to the foliation.

381 Table 1. Deformation temperature estimates of microstructures and quartz C-axis fabrics.

Sample number	**Lithology**	**Mineral compositon**	**Mineral deformation behavies**		**Quartz C-axis fabric pattern**	**Deformation temperature estimates/°C**
			Quartz	Feldspar		
Profile B-B'						
ALYJ1617-1	two-mica schist	Feld+Q+Mus+Bt	SGR+GBM; rectangular quartz ribbons	BLG+SGR	Y-axis maxima; small-circle girdle	550-650°C; 400-500°C
ALYJ1617-2	muscovite schist	Feld+Q+Mus	SGR+GBM	BLG+SGR	Y-axis maxima; Z-axis sub-maxima	550-650°C; 350-450°C
ALYJ1618-4	two-mica schist	Feld+Q+Mus+Bt	SGR+GBM; rectangular quartz ribbons	BLG+SGR	Y-axis maxima; Z-axis sub-maxima	550-650°C; 350-450°C
ALYJ1622-3	metamorphic sandstone	P (40%): Q+Feld M (60%): Feld+Q+Bt	SGR; BLG	BLG; brittle fracture	small-circle girdle; Z-axis sub-maxima	350-450°C; <350°C
ALYJ1624-	phylite	P (15%): Q+Feld	BLG; undulose	brittle fracture	Z-axis sub-maxima	400-450°C

6		M (85%): Feld+Q+Ser P (30%): Q+Feld	extinction			
ALYJ1625-3	phylite	M (70%): Feld+Q+Bt	BLG+CM; undulose extinction	brittle fracture	Z-axis sub-maxima; small-circle girdle	400-450°C; <350°C

P–porphyroclast；M–matrix；Q–quartz; Feld–feldspar; Mus–muscovite; Bi–biotite; Mi–mica; CM–core and mantle structure; BLG–bulging recrystallization；SGR–subgrain rotation recrystallization；GBM–grain boundary migration.

382

3.3 Vorticity analyses

Vorticity analysis has been frequently used to evaluate the degree of non-coaxiality of strain and to reconstruct the non-steady-state deformation histories of naturally deformed rocks in shear zones from different settings (Wallis, 1995; Grasemann et al., 1999; Wagner et al., 2010; Xypolias et al., 2010; Law et al., 2013; Ring et al., 2015). For plane strain deformation, components of pure shear and simple shear can be quantified in terms of the kinematic vorticity number Wk (Means et al. 1980). In cases of non-steady-state deformation, flow is more appropriately characterized by the mean kinematic vorticity number Wm, in which the vorticity of flow is integrated over space and time (Passchier, 1987). For steady-state deformation Wk (instantaneous deformation) is equal to Wm (finite deformation). Quantitative vorticity analyses can be performed using a range of methods (Wallis, 1992; Simpson & De Paor, 1993; Tikoff and Fossen, 1995; Grasemann et al., 1999; Xypolias, 2010). We here attempt to use the rotated rigid porphyroclast method in vorticity analysis of the ALTB samples. This method proposed by Wallis et al. (1993) is based on measuring the orientation and aspect ratio of rigid porphyroclasts rotating in homogeneously deformed matrix, and finding a critical aspect ratio (Rc) below which porphyroclasts continuously rotate and hence their long axes display no finite preferred alignment, and above which they achieve stable end orientations. A first-order requirement to using this method is that no mechanical interaction between porphyroclasts (Passchier 1987; Tikoff & Teyssier 1994). Eight representative samples are selected for vorticity analysis whose sampling locations are shown in Figure 8. All thin sections perpendicular to foliation and parallel to lineation are photographed under a microscope, and these images are processed by using the software “ImageJ” to obtain orientation (θ) and aspect ratio (R) of rigid porphyroclasts. Vorticity is obtained by plotting R versus θ on a Wallis plot to define Rc and is calculated by equation from Passchier & Trouw (2005). The results are expressed in terms of mean kinematic vorticity number Wm.

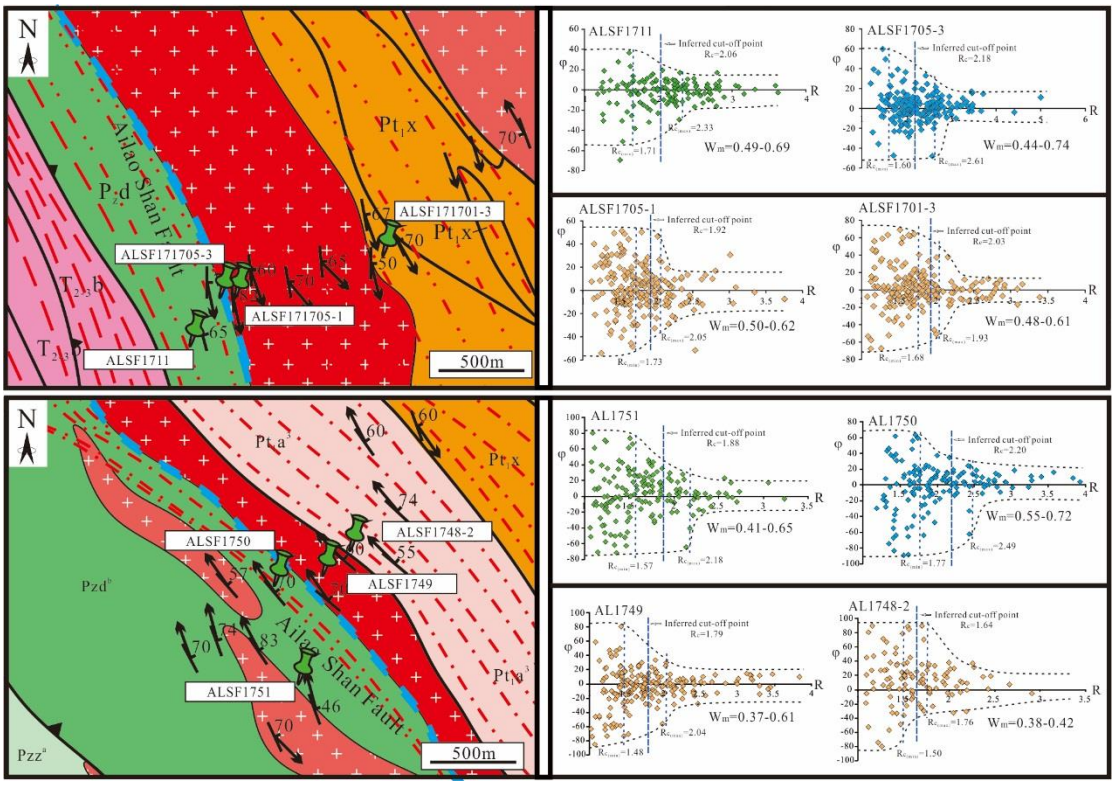

Figure 8. Wills diagram of rotated rigid porphyroclast vorticity analysis in the northern segment of ALTB (Figure legends refer to Figure 2).

Mean vorticity (Wm) estimates in eight samples are shown in the Figure 8. Four of eight samples are porphyritic granitic mylonites with well-preserved magmatic idiomorph from the HMU (i. e., ALSF1701-3, ALSF1705-1, AL1748-2, and AL1749). Estimated Wm values for these samples range from 0.42 to 0.69 (72-52% pure shear component; Figure 8, Law et al., 2004).Two of eight samples (i. e., ALSF1711 and AL1751), sampled from the LMU, are metasandstone with porphyroclasts embedded in a fine-grained quartz-mica matrix. Wm values estimates of them range from 0.37 to 0.62 (76-58% pure shear component; Figure 8, Law et al., 2004). The vorticity values mentioned above indicate that both the HMU and LMU are characterized by dominantly general shear with a larger component of pure shear. Besides, two samples (i. e., ALSF1705-3 and AL1750) of phyllonites characterized by long-axis of porphyroclasts subparallel to the foliation plane were also used to measure the kinematic vorticity. The estimated Wm values range from 0.44 to 0.74 (71-47% pure shear component; Figure 8, Law et al., 2004), indicating a larger component of simple shear than that of the other two units.

4 Deformation temperature estimations

The syn-structural minerals are critical indictors that preserving some of the information related to temporal deformation P-T conditions. It can be used to assess the crustal level of the rocks deformed and its rheological state. Therefore, we select different syn-structural minerals to construct the thermometers, further to obtain the deformation temperature in the HMU and the LMU, respectively.

4.1 Deformation temperatures in the high-grade metamorphic unit (HMU)

Within the HMU, two-mica schists adjacent to the ultramylonite belt show well-developed mylonitic foliation and stretching lineation. Stable mineral assemblages and textural equilibria are preserved in our two-mica schist samples (i.e., ALYJ1617-1, ALYJ1618-4), whose deformation microstructures and quartz C-axis fabrics were shown in the last chapter. Here, it's important to emphasize that the micas are deformed related to the mylonitic event and do not show textures of retrograde reaction. Ilmenite grains are visible around the micas, indicating that Ti is saturated in the system.

Three techniques are employed to provide an assessment of the deformation temperature in the HMU: Ti-in-biotite thermometry, Ti-in-muscovite thermometry and muscovite-biotite thermometry. Ti-in-biotite thermometry temperature was calculated following the empirically calibrated formulation described in Wu et al. (2015a). The Ti-in-biotite thermometry was developed for metapelites that contain a Ti-saturating phase. Wu et al. (2015a) determined the thermometry is consistent with the well-calibrated garnet–biotite thermometer within an error of ±50 ℃ for most of the calibrant samples (450–840 ℃, 0.1–1.9 GPa, X_{Ti} = 0.02–0.14 in biotite). Ti-in-muscovite thermometry empirically calibrated by Wu et al. (2015b) can be applied to TiO_2-saturated, ilmenite- and Al_2SiO_5-bearing natural metapelites in the temperature range of 450–800 ℃ to muscovites within the cation ranges of Ti = 0.01–0.07, Fe = 0.04–0.16, Mg = 0.01–0.32 and Mg/(Mg+Fe)=0.05–0.73 of muscovites for estimating the metamorphic temperature conditions of low- to medium-grade metapelites. Muscovite-biotite thermometry is based on the exchange of Mg-Tschermak's component between muscovite and biotite. It was calibrated by

Hoisch (1989) for metapelitic assemblages under P-T conditions of 0.2–0.96 GPa and 450–700 ℃. Applications of the muscovite-biotite thermometry should be restricted to micas that are compositionally similar to those calibration data used in Hoisch (1989). The three above techniques are irreplaceable to natural metapelite samples devoid of garnet or plagioclase. Experimental results have demonstrated that Ti contents of the minerals appear to be weakly correlative with pressure (Wu et al., 2015a, b). Here, we assume a range of the pressure from 0.4 GPa to 0.6 GPa based on predecessors' research literature (Leloup & Kienast, 1993; Gilley et al., 2003; Leloup et al., 2007; Ji et al., 2016).

JEOL JXA-8230 electron microprobe at the Electron Probe Laboratory of Shandong Bureau of China Metallurgical Geology Bureau was used to acquire mineral chemical data for Ti-in-biotite thermometry, Ti-in-muscovite thermometry and muscovite-biotite thermometry. The operating conditions were set to 15 kV accelerating voltage, with a beam current of 10 or 20nA, and the beam spot of 10μm. For standardizing, natural samples were used. The standard sample adopts the American SPI Mineral/Metal Standard and China National Standards. Microprobe analysis was performed on the core and mantle of mica grains. The mineral chemical data are list in Appendix A.

Calculated temperatures using thermometry calibrated by Wu et al. (2015a, b) and Hoisch (1989) are plotted on the T versus P diagram (Figure 9) Deformation temperature estimates on the core and mantle of mica grains show similar temperature values. There are no characteristics of multi-stage temperature values, indicating that the micas in the test samples were deformed in the same period. Ti-in-biotite thermometry, applied to sample ALYJ1617-1, shows a wide variation in temperatures, from 676 ℃ to 741 ℃ (at the assumed pressure of 0.4~0.6 GPa). The sample ALYJ1618-4 appears to record hotter deformation temperatures of 680~834 ℃. Application of the Ti-in-muscovite thermometry to sample ALYJ1617-1 and ALYJ1618-1 yielded the deformation temperatures of 610~701 ℃ and 618~645 ℃ (assuming the pressure ranges from 0.4 GPa to 0.6 GPa), respectively. Muscovite-biotite thermometry was also used to place constraints on the deformation

temperature of the above two samples. Calculated temperatures are 645~738 ℃ and 631~678 ℃ under the same assumed pressure. Here a large uncertainty (±50 ℃) is applied to account for the error from experiment and calculation. We can propose an approximate deformation P-T condition of 610~834 ℃, 0.4~0.6 GPa.

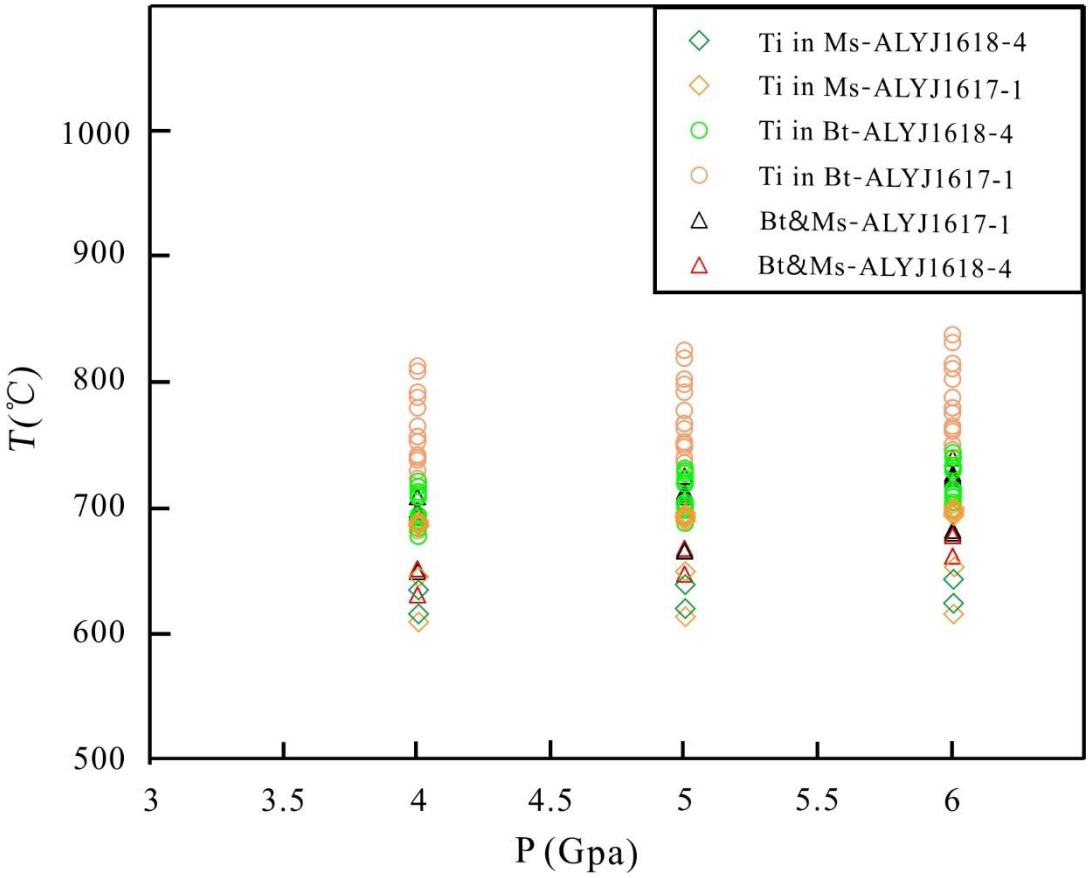

Figure 9. Histograms of homogenization temperatures and salinities of fluid inclusions in quartz veins from LMU.

4.2 Deformation temperatures in the low-grade metamorphic unit (LMU)

Syntectonic quartz veins are widely distributed in the LMU, especially the area adjacent to the ALSF. These veins exhibit a width of less than 1 cm and are shaped as spindles, or lenticel and rootless folds. The folded vein develops the stretching lineation paralleling to the hinge and the regional stretching lineation. The quartz grains under microscope rarely show crystal plastic deformation and the evidence of BLG is preserved locally. Wall rocks constitute of phyllite with well-developed cleavage. We interpret that the quartz veins in phyllite probably experience a progressive deformation process, which were developed and deformed simultaneously with mylonitization Therefore, we utilize the primary fluid inclusions in the

syntectonic quartz vein to estimate temporal deformation temperature.

The thermormometric study of fluid inclusions trapped syntectonic quartz veins was performed using a Linkam MDS600 heating and freezing system with a German Leica microscope at the MLR Key Laboratory of Metallogeny and Mineral Assessment, Institute of Mineral Resources, Chinese Academy of Geological Sciences (CAGS). Thermocouples were calibrated in the range of -196 ℃ to 600 ℃ using synthetic FIs. The precision of temperature measurement is ± 1 ℃ in the range of -100 ℃ to 400 ℃, and ± 2 ℃ for temperatures above 400 ℃. The heating rate was general 15-20 ℃/min during the process of fluid inclusion testing but reduced to 1-5 ℃/min when reaching the freezing point, and to 0.5-1 ℃/min near the homogenization temperatures to record phase transformation processes accurately.

Primary fluid inclusions are abundant in the quartz vein of two samples from the low-grade metamorphic unit. Microscopic and microthermometric observations display the inclusions are irregular or elliptical with the grain size ranging from 5μm to 10μm. The vast majority of primary inclusions show two dominant fluid phases at room temperature (Figure10): a liquid phase (L) and a vapor bubble (V). Liquid to vapor ratio is unconstant from 15% to 60% (Appendix B). Final ice melting temperatures of primary aqueous inclusions in sample ALYJ1621-1B range from −0.2 ℃ to −2.9 ℃, corresponding to salinities from 1.6 to 3.2 wt.% NaCl equiv, with an average of 2.3 wt.% NaCl equiv. Temperatures of homogenization to liquid phase for all fluid inclusions vary from 210.8 ℃ to 381.2 ℃, mostly between 320 ℃ and 380 ℃ (Figure 10). Sample ALYJ1621-2B, from which primary inclusions have ice-melting temperatures (Tm) from −0.2 ℃ to −2.3 ℃, corresponding to salinities of 0.35 to 3.87 wt.% NaCl equiv, with an average of 1.65 wt.% NaCl equiv. Temperatures of homogenization to the liquid phase of these fluid inclusions range from 233.9 ℃ to 391.9 ℃, mostly between 345 ℃ and 390 ℃ (Figure 10). The lack of polyphase liquid inclusions in those samples makes it difficult to get the trapping temperature by pressure calibration. Thus, we presumed the maximal homogenization temperature of 391.9 ℃ to represent the upper limit of deformation temperature in the LMU.

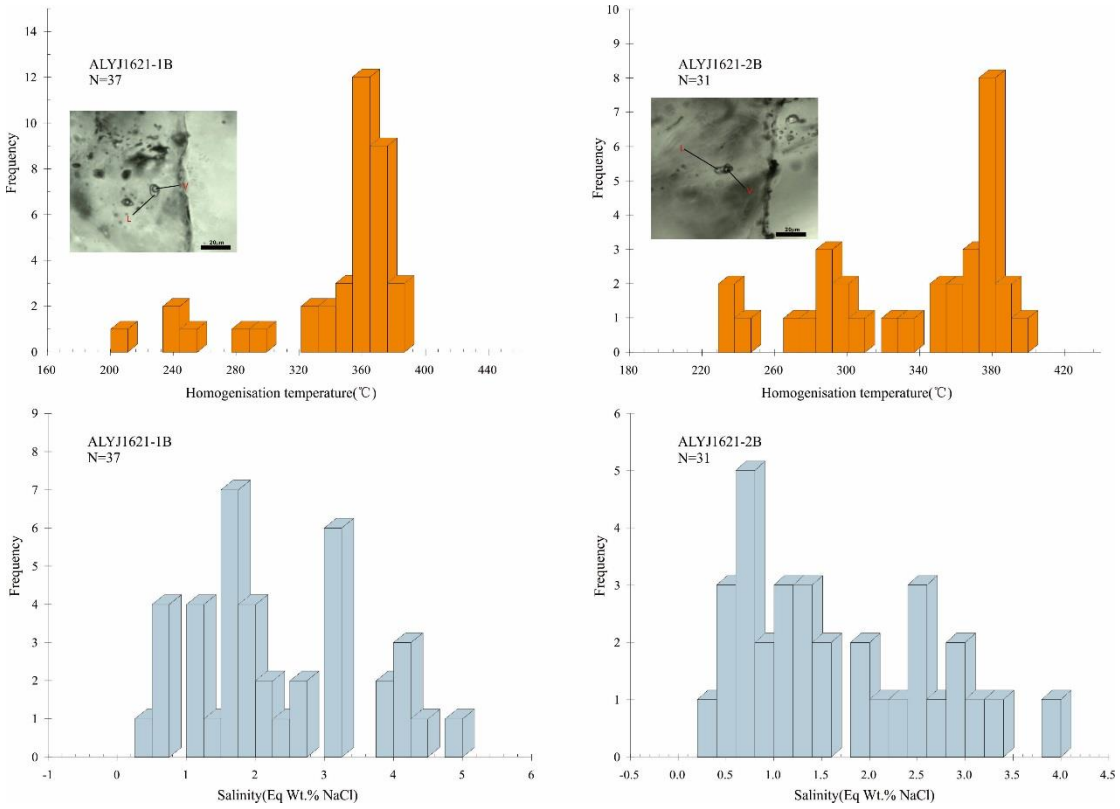

Figure 10. Temperature-pressure diagram of calculated temperatures in the HMU by using Ti-in-biotite thermometry, Ti-in-muscovite thermometry and muscovite-biotite thermometry.

5 Discussion

5.1 Previous structural interpretations of the Ailao Shan fault

The 800 km-long ALSF was defined as a fault that separates two units with contrasting metamorphic grades (Leloup et al., 1995). Gravity and magnetic survey reveals some distinct anomalies along the fault zone but poorly in integrity and continuity (BGMRY, 1990). LANDSAT and SPOT images also show that the ALSF is a regional discontinuity offsetting the high-grade metamorphic rocks in the northeast over several tens of kilometers long (Leloup, 1991), although it is actually difficult to find the exact fault trace at the outcrops. The fault is composed of phyllonites and ultramylonites with stretching lineations consistent with the fault strike. A large amount of evidence for left-lateral shearing is preserved. A-type folds have hinge lines paralleling the NW-SE-plunging stretching lineations in the folded mylonitic rocks. At the Mojiang-Xinping area, the northern segment, the fault strikes approximately NW-SE and dips to the northeast with a dip angle ranging from 60° to 70°, while to

552 the south, the fault trends NWW in most places dips steeply to NE with a dip angle of
553 40-80°. It was suggested that the fault has trust-fault or transpressional features
554 consistent with NE-SW shortening (BGMRY, 1990).

555 The ALSF could be one of the major faults related to multi-stage tectonic
556 activities in Yunnan Province (BGMRYP, 1990). Its early stage of activity was
557 interpreted as of compressional or transpressional with the development of mylonites
558 and phyllolites, while its late stage faulting is characterized by transtensional activity.
559 Leloup et al. (1995) referred to the ALSF as a thrust fault that results in the HMU
560 thrusted upon the LMU. Zhang et al. (2006) argued that the faulting along the ALSF is
561 oblique thrust faulting with left-lateral strike-slipping component.

562 However, there have been controversies on the structural attributes of the fault.
563 More importantly, rare evidence of brittle faulting is found at the outcrop along the
564 fault. Allen et al. (1984) suggested that the fault may represent part of an ancient plate
565 boundary. Some Mesozoic ultrabasic-basic rocks and small intermediate-acidic
566 intrusions crop out to the adjacent fault zone, which is also attributed to its long
567 history of activity since the Mesozoic (Zhong et al., 1998; Searle, 2010; Deng et al.,
568 2014). Recently, the possible location of the Ailao Shan suture zone was defined
569 (Wang et al., 2014), a mélange to the southwest of the ALSF. These Mesozoic
570 subduction-collision related igneous rocks along the ALSF are neither linearly
571 distributed nor cut by faults.

572 5.2 The Ailao Shan tectonic discontinuity

573 Detailed structural mapping and field investigation along three cross-sections
574 across the northern segment of the ALTB reveal that structural elements associated
575 with a brittle fault, such as the major fault surface, cataclasites or fault gouges, are
576 lacking at the previously defined location of ALSF. Instead, an ultramylonite belt of
577 ca. 300 to 1000m wide is observed between the HMU and the LMU. Mylonitic fabrics
578 of a high-stain zone are popular within the belt, evidenced by strongly foliated
579 phyllonites with subhorizontal stretching lineations parallel to the strikes of the
580 foliations. According to mesoscopic observations and the results of kinematic vorticity
581 analysis, here it is concluded that the high-strain zone represents a middle crustal

582 shear zone of dominant simple shear components.

583 The shear zone separates two units (i.e. HMU and LMU) with identical structural
584 and kinematic characteristics but contrasting metamorphic grades. Rocks in the two
585 units are generally experienced solid-state plastic deformation. Definitely, two-stage
586 deformation is identified in our contribution. The early-stage deformation is inferred
587 to as ubiquitous steep foliation and sub-horizontal stretching lineation. The fault rocks,
588 e.g., the S- or S>L type tectonites are characterized by intensive mylonitization
589 resulted from deformation related to plane strain with dominant pure shear component.
590 In the late stage, deformation is non-penetrative and localized on some high-strain
591 zones with simultaneous NW-SE oriented anticlockwise and top-to-the-southwest
592 shearing. Syn-shear folding contributed to the formation of A-type folds. The folded
593 layerings are preexisting mylonitic bandings (S_{0+1}) in the HMU and phyllonitic
594 cleavages (S_1) filled with syntectonic quartz veins in the LMU, respectively. The
595 deformation microstructures and quartz C-axis LPO fabrics analyses imply that rocks
596 in the HMU were deformed at temperatures above 550 ℃ (Figure 11), coupling with
597 the deformation mechanisms of subgrain rotation or grain boundary migration
598 dynamic recrystallization (Passchier & Trouw, 2005; Law, 2014). In contrast, the
599 highly sheared rocks in the LMU show deformation microstructures consistent with
600 dominant deformation mechanism of dislocation creep while the quartz C-axis LPO
601 fabrics imply a low-temperature deformation at 400-350 ℃ (Figure 11, Passchier &
602 Trouw, 2005; Law, 2014). Furthermore, the homogenization temperature
603 measurements using fluids inclusions from quartz veins in the phyllonite give an
604 upper limit of deformation temperatures at ca. 400 ℃ in the LMU. However,
605 integrated Ti-in-biotite thermometry, Ti-in-muscovite thermometry and
606 muscovite-biotite thermometry yield the deformation P-T condition of 610~834 °C,
607 0.4~0.6 Gpa (Figure 11). We, therefore, conclude from the above data that the ALSF
608 is a major mid-crustal tectonic discontinuity (TDC) between the HMU and the LMU,
609 instead of being a brittle fault. It is expected that some secondary tectonic
610 discontinuities are also developed within both the HMU and LMU rocks (Figure 12).
611 Further quantitative analysis is needed in future studies.

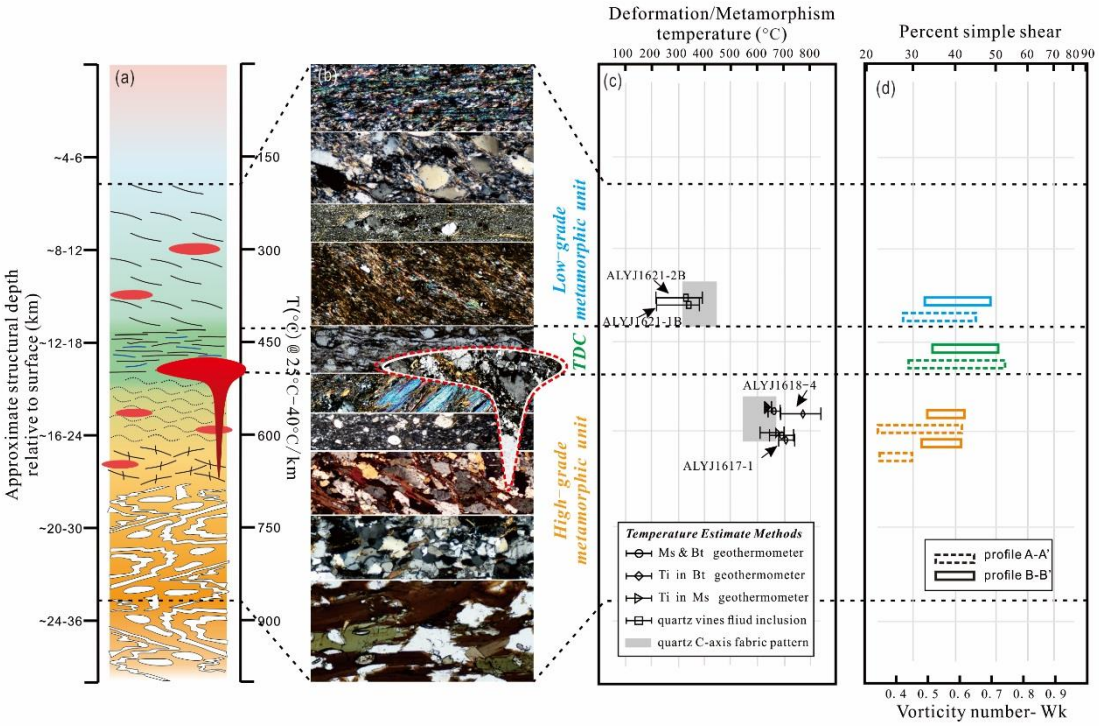

Figure11. Ideal model of the exposed crustal profile in the northern ALTB. The graph illustrates the lithological compositions and deformation behaviors at different crustal levels, the deformation temperature estimates between the HMU and the LMU, and the variation of vorticity number.

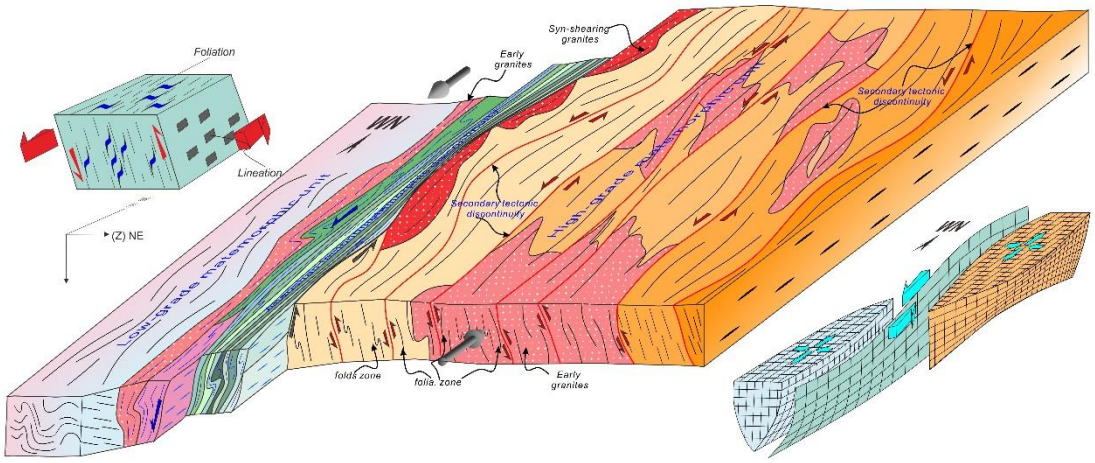

Figure 12. Three-dimensional structural model of the northern ALTB and the mid-crustal tectonic discontinuity contact. This model presents the structural geometries, kinematics and deformation characteristics for mid-crustal tectonic discontinuity contact.

5.3 Mechanisms for the formation of the ALS TDC

In recent years, multidisciplinary approaches through integrated geological mapping, structural analysis, petrology, and geochronology studies, allow us to well

624 constrain the internal architecture of previously defined fault zones. The most evident
625 example is the finding of mid-crust tectonic and metamorphic discontinuities,
626 recognized and mapped in many different localities at the Central and Eastern
627 Himalaya (Montomoli et al., 2013, 2015 and references therein), and at the
628 Southeastern Tibetan Plateau (Chen et al., 2016, 2017; Yan et al., 2021). The
629 discontinuities were described as high-strain zones separating distinguishable
630 protoliths of contrasting metamorphic grades. Intensive strain-localization along the
631 TDC may lead to incision of the crustal thickness.

632 It is clear from semi-quantitative and quantitative approaches in this study that
633 rocks that the abrupt change in deformation characteristics and inferred P-T
634 conditions of deformation is attributed to the existence of a TDC between the two
635 units. Such a TDC occurred at the middle to lower crustal transition may have
636 contributed to the juxtaposition of different rock units from different crustal levels.
637 Our results highlight three key issues on the mechanisms of occurrence of the ALS
638 TDC.

639 5.3.1 The significance of the cover/basement contact

640 The role of the pre-existing cover/basement contact may have controlled the
641 geometry of deformation at various tectonic settings, which have been documented in
642 many previous examples of various tectonic settings (Thomas, 1990; Burchfiel et al.,
643 1992; Nelson et al., 1996; Beaumont et al., 2001; Montomoli et al., 2013; Chen et al.,
644 2016; Liu et al., 2017; Yan et al., 2021; Zheng et al., 2021). Typically, the thin-skinned
645 thrusting in Appalachian Mountains is largely controlled by a basal décollement
646 between the Paleozoic strata and the Proterozoic crystalline basement (Thomas, 1990).
647 In the Himalaya, the Southern Tibet Detachment (STD, Burchfiel et al., 1992) was
648 triggered, at least in part, by partial melting of underlying Himalaya thrust wedge
649 (Nelson et al., 1996) between the thick Tethyan sedimentary cover and the underlying
650 crystalline basement of up to upper amphibolite to granulite facies metamorphism
651 (Montomoli et al., 2013). The detachment further enabled the southward extrusion of
652 a thick, mid-crustal channel, over distances of well over 100 km, during the Miocene
653 (Beaumont et al., 2001). Such tectonic discontinuities have been recently recognized

654 from the Yao Shan complex (Chen et al., 2016) and Diancang Shan complex (Yan et
655 al., 2021), southeastern Tibetan Plateau. They were formed as the consequence of
656 shearing along a pre-existing contact separating the highly-sheared proterozoic
657 crystalline protolith and the Paleozoic sedimentary rocks. Additionally, studies on
658 crustal-scale extensional structures, for example, the Liaonan MCC by Liu et al.
659 (2017), Zheng et al. (2020) reveal that an obvious tectonic discontinuity contact (TDC)
660 exists between a lower unit of sheared Archean gneisses and an upper unit of sheared
661 Neoproterozoic meta-sedimentary rocks. Rocks below and above the TDC possess
662 structures and fabrics with consistent geometries and kinematics. A metamorphic
663 break exists between the two units that were sheared at contrasting deformation
664 conditions.

665 The ALSF may have provided another important candidate that characterizes
666 control of pre-existing stratigraphic unconformity on the occurrence of a TDC during
667 ductile flow at the middle to lower crust transition. Regional geological correlation
668 reveals that the HMU and LMU are equivalent to the crystalline basement rocks and
669 volcanic-sedimentary cover rocks. The former is composed of highly-sheared
670 proterozoic crystalline protolith while the latter comprises the Silurian to Middle
671 Triassic sediment. A regional uncomformity contact between the cover and basement
672 is proved to exist in comparison with the stratigraphic sequence of its periphery region
673 such as the Yangtze block, which consists of Precambrian metamorphic complexes
674 overlain by a thick (>10 km) sequence of late Neoproterozoic (Sinian) to Cenozoic
675 cover rocks (Zhou et al., 2002). The cover/basement contact, where present,
676 commonly corresponds to changes in constituents, metamorphic grades and
677 deformation characteristics with stratigraphic horizons. Typically, gneissic rocks in
678 the basement are characterized by high-grade metamorphism when the magmatite
679 reveals the lower crustal partial melting. All the rocks display mylonitic features of
680 well-developed foliation and lineation, especially adjacent to the ALSF, showing
681 typical deformation characteristics of mid-lower structural level. The layered cover
682 sequence develops a sequence of sediments that experienced low-grade
683 metamorphism but identical shearing to those in the HMU. These rocks exhibit

deformation characteristics at shallow structural level with representative open folds, and the brittle faults as well. Previous studies revealed that the metamorphism and deformation in both HMU and LMU occurred at Oligo-Miocene (30 to 21 Ma, Liu et al., 2020 and references therein). The contact between the HMU and LMU, thus, can be inferred as a "décollement" during ductile shearing, which is commonly reported in orogenic belt that decouples the cover sequences from crystalline basement (Harris & Milici 1977; Thomas 1990; Searle et al., 2008).

Thus, the role of cover/basement contact may be potentially explained by different deformation styles and metamorphic characteristics at the HMU and LMU. The increase in deformation temperatures and metamorphic degrees from the LMU to HMU may have led to the transition of semi-ductile to ductile deformation in the middle crust. Tectonic reactivity of the unconformity contact formed the ALS TDC, a zone of strain localization favored by the high viscosity contrast between the mechanically rigid underlying basement and the detached sedimentary cover.

5.3.2 Stratified subhorizontal flow in the middle-lower crust

Several lines of evidence suggest that the ALTB represents a tilted crustal section that was characterized by stratified subhorizontal flow in the middle-lower crust. Metamorphic assemblages and structural associations of the different units from the ALTB obviously changes with stratigraphic horizons. The HMU is interpreted to represent the exhumed middle-lower crustal basement core. Correspondingly, the LMU is interpreted to be a sequence of deformed rocks at relatively shallow crustal level. The middle-lower and middle-upper crustal rocks are generally characterized by solid-state plastic flow, while shearing at the lower crust is accompanied by migmatization and partial melting. Shear fabrics are common in both the HMU and LMU. Sheared rocks in the units have foliations parallel to each other and they are concordant with the orientation of the unit boundaries. Stretching lineations on the foliation surface are generally subhorizontal in the studied cross-sections. In addition, shear indicators are ubiquitous in the sheared rocks from both units and the ultramylonite zone. Vorticity estimates in this study associated with ductile deformation in the ALTB decrease from HMU to LMU, indicating an increase in pure

714 shear component from 72-52% in the HMU, to 76-58% in the LMU (Figure 11). The
715 increase in pure shear component was ascribed to an increased lithostatic load with
716 the increase of structural depth (Wagner et al., 2010). However, the simple shear
717 component of phyllonite within the TDC is 29-53%, which is apparently higher than
718 that from two adjacent units, corresponding to a celerating strain path during
719 progressive deformation. The above data suggest that the HMU and the LMU at
720 presently exposed level were kinematically linked while mechanically decoupled
721 during subhorizontal shearing in Oligo-Miocene.

722 Stratified flow is one kind of the most common structural expressions of
723 orogenic belts, which is attributed to elevated heat flow with strong anisotropic
724 characteristics (Royden et al., 1997; Liu et al., 2020). Seismic anisotropy revealed by
725 the high-resolution tomographic images demonstrates a regional crustal flow that has
726 intruded northeastward into NE Tibet, which is responsible for the intracrust and
727 crust-mantle decoupling (Sun & Zhao, 2020). Chen et al. (2016, 2020) proposed that
728 the middle-upper crust flew or slid at a higher velocity than the lower crust, not only
729 the boundary faults but in the plate interior of the Sundaland block, being compatible
730 with the present observations of top-to-the south kinematics during the tangential
731 shearing in Southeast Tibet. In such a case, the former basement/cover contact
732 represents a priority to be inherited as a decollement during progressive shearing.

733 5.3.3 Crustal incision and regional doming

734 Integration of quartz c-axis fabric pattern and conventional geothermometry data
735 emphasizes the existence of a metamorphic discontinuity between the HMU and LMU,
736 characterized by a temperature difference of ca. 200°C. Assuming an average
737 geothermal gradient of ca. 30°C/km within the ALTB (Leloup et al., 1993; Leloup &
738 Kienast, 1993; Wintsch & Yeh, 2013), such a temperature range may imply that
739 crustal masses of nearly 6 km were incised along the TDC during Cenozoic
740 exhumation. How the crustal masses in the middle crust were lost during the
741 subhorizontal shearing thus remains a first-order question in understanding the
742 mechanisms of flow of middle to lower crustal rocks.

743 Recent studies revealed that three of the four high-grade complexes, i.e., the

744 Xuelong Shan, Diancang Shan and Yao Shan-Day Nui Con Voi constitute elongated
745 regional domal structures (Chen et al., 2016; Zhang et al., 2017a; Yan et al., 2021).
746 They are formed by cores of high-grade crystallin rocks and mantles of low-grade
747 metasedimentary sequences. From the structural geometry and kinematic analysis,
748 some of them are defined as A-type domes. Exhumation of high-grade cores of the
749 domes was suggested to be attributed to regional doming by subhorizontal ductile
750 flow (Chen et al., 2016; Yan et al., 2021). Vertical components of high-strain shearing
751 led to doming and exhumation of the high-grade cores. Middle to lower crustal rocks
752 sheared at high-temperature conditions were progressively exhumed to shallower
753 levels and further sheared at low-temperature conditions. Low-grade rocks at the
754 middle-upper crustal level were sheared and superimposed by progressive
755 deformation at low temperatures.

756 The above tectonic scenario also applies to the shearing and exhumation of the
757 high- and low-grade metamorphic rocks and formation of the ALS TDC in the ALTB.
758 The scenario starts with a horizontally layered crust where five units constitute the
759 thick pile of the crustal masses: unit *i* in the upper crust is characterized by brittle
760 deformation, unit *ii* to *iii* correspond to the middle crustal brittle-ductile transition
761 zone, high-grade metamorphic rocks of Proterozoic protoliths and migmatized lower
762 crust, respectively. The brittle upper crust and the ductile middle-lower crust separated
763 between greenschist facies and amphibolite facies or higher grades. The unit
764 boundaries are marked by distinction of rheological characteristics. For reasons of
765 preexisting basement/cover contact between unit *i* and *iii*, the middle-lower crust
766 is mechanically decoupled with upper crust during stratified subhorizontal flow. The
767 kinematic indicators such as asymmetric A-type fold and quartz vein suggest that
768 main phase of regional doming in Oligo-Miocene accompanied dominant top-to-the
769 southwest upper crustal shearing with a vertical component. The upper units together
770 with transition zone (unit *ii*) are usually tilted and displaced to the flanks of the
771 dome. The former is eroded and deposit in periphery Cenozoic basins while the latter
772 experiences the maximum stretching and necking internally, possibly, owing to
773 fluid-related weakening (i. e., syntectonic quartz vein), and then low shear strength

and increasing strain localization (i. e., formation of ultramylonite). It is tenable for the occurrence of TDC at the transition zone where large parts of the original crustal masses can be removed through incision. This process also forms the highly sheared high-grade core with lateral strike-slip shear zones at its flanks. In the final structure of ALTB, low-temperature deformed LMU rocks (unit *i*) are directly juxtaposed with the deep crustal levels (units *iii*). A possible explanation for the present monoclinic structure of ALTB may be that the destruction of RRF for its component of down-to-the-NE normal displacement.

5.4 Tectonic implication

It is shown from multidisplinary studies that there are several lithological and structural discontinuities at different levels of the continental lithosphere, i.e., the Moho, the Conrad discontinuity, and various middle-lower crustal subhorizontal low-velocity and high-conductivity zones (LV-HCZs). Most of the discontinuities are contacts or transitions of contrasting petrological and/or rheological layers. Widespread LV-HCZs in the middle crust contribute to occurrence of the seismic anisotropy in the crust beneath NE Tibet (Sun & Zhao, 2020). The occurrence of the middle crustal LV-HCZs has been attributed to partial melting, existence of aqueous fluids (e.g., Wei et al., 2001), occurrence of crustal shear zones (e.g., Tapponnier et al., 2001), or the presence of carbon films along grain boundaries of minerals (e.g., Yoshino & Noritake, 2011 and references therein) in the middle crust.

The Ailao Shan TDC highlights the importance of middle crustal strain-localization that contributes significantly to the transition of flow characteristics of the upper crust and middle-lower crust. As discussed above, middle crustal strain-localization evidenced by occurrence of TDCs is ubiquitous around the southeastern and central Tibetan Plateau. As a result, the occurrence of strain-localization couples with weakening of middle crustal rocks, high strain accumulation and local increasing of strain rate (Read & Hegemier, 1984). The above processes significantly contribute to the formation of middle crustal weak zones that possess specific geological characteristics. Intensive grainsize reduction, strengthened foliations and high degrees of fabric development in the weak zones may control the

seismic anisotropy of rocks in the middle crust (McDonough & Fountain, 1988). The conclusion is supported by existence of low shear-wave velocity zones or high-conductivity layers revealed by previous seismic studies (Kind et al., 1996; Wei et al., 2001; Sun & Zhao, 2020). The prominent low-velocity zones are coincident with strong mid-crustal radial anisotropy in western and central Tibet, which is ascribed to the effects of anisotropic minerals aligned by deformation (Yang et al., 2012). We would therefore argue that, the existence of middle crustal TDC provides a possible explanation for occurrence of middle crustal low-velocity and high-conductivity zone in the southeastern Tibet Plateau, where strain-localization determines the geological, rheological and geophysical behaviors of the middle crust.

6 Summary and conclusions

New field, and microstructural observations, kinematic vorticity analysis, quartz C-axis fabric patterns and thermometry results allow us to redefine the 'Ailao Shan fault' as a mid-crustal tectonic discontinuity (TDC). The following conclusions are drawn from the present study:

(1) Along the previously defined 'Ailao Shan fault', an ultramylonite belt or TDC represents a middle crustal strain-localization zone of general shear with a higher simple shear component (29-53%) than adjacent rock units (28-48% in the HMU and 24-42% in the LMU).

(2) Rocks in the HMU and LMU below and above the TDC possess identical structural and kinematic characteristics but contrasting metamorphic grades. The contrast between the high deformation temperatures in the HMU (650-550°C) and low deformation temperatures in the LMU (400-350°C) from deformation microstructures and fabrics are supported by geothermometry results, i.e., of 610 ~834°C, 0.4~0.6GPa in the HMU and the upper limit of deformation temperature of ca. 400 °C in the LMU.

(3) Rocks from different crustal levels are juxtaposed along the TDC in response to the extrusion of the Sundaland block. The TDC inherited preexisting basement/cover contact of ALTB and reactivated during progressive stratified middle to lower crustal flow in Oligo-Miocene. Contemporaneously, doming

during lower crustal flow resulted in exhumation of the lower crustal rocks and incision of crustal masses in the middle crust.

(4) The ubiquitous occurrence of TDCs provides a possible explanation for the middle crustal low-velocity and high-conductivity zone in the southeastern Tibet Plateau, where strain-localization determines the geological, rheological and geophysical behaviors of the middle crust.

Acknowledgments and data availability statement

This study is funded by the National Science Foundation of China (Grant No. 41430211 and 91955205). The appendix A and B can be obtained via https://osf.io/qt4rm/.

References

Allen, C. R., Han, Y., Sieh, K. E., Zhang, B., & Zhu, C. N. (1984). Red River and associated faults, Yunnan Province, China: Quaternary geology, slip rates, and seismic hazard. *Geological Society of America Bulletin,* 95, 686– 700. https://doi.org/10.1130/0016-7606(1984)95<686:RRAAFY>2.0.CO;2

Anczkiewicz, R., Viola, G., Muentener, O., Thirlwall, M. F., Villa, I. M., & Nguyen, Q. Q. (2007). Structure and shearing conditions in the Day Nui Con Voi Massif: Implications for the evolution of the Red River shear zone in northern Vietnam. *Tectonics,* 26(2), TC2002. https://doi.org/10.1029/2006TC001972

Bai, D. H., Unsworth, M. J., Meju, M. A., Ma, X. B., Teng, J. W., Kong, X. R., Sun, Y., Sun, J., Wang, L. F., Jiang, C. S., Zhao, C. P., Xiao, P. F., & Liu, M. (2010). Crustal deformation of the eastern Tibetan Plateau revealed by magnetotelluric imaging. *Nature Geoscience,* 3 (5), 358– 362. https://doi.org/10.1038/ngeo830

Beaumont, C., Jamieson, R.A., Nguyen, M.H., & Lee, B. (2001). Himalayan tectonics explained by extrusion of a low-viscosity crustal channel coupled to focused surface denudation. *Nature*, 414(6865), 738– 742. https://doi.org/10.1038/414738a

BGMRYP (Bureau of Geology and Mineral Resources of Yunnan Province) (1990). *Regional geology of Yunnan Province.* Beijing, China: Geological Publishing House.

Blumenfeld, P., Mainprice, D., & Bouches, J.L. (1986). C-slip in quartz from subsolidus deformed granite. *Tectonophysics*, 127, 97– 115. https://doi.org/10.1016/0040-1951(86)90081-8

Burchfiel, B. C., Chen, Z., Hodges, K. V., Liu, Y., Royden, L. H., Dong, C. R., & Xu, J. N. (1992). The South Tibetan detachment system, Himalayan Orogen: extension con-temporaneous with and parallel to shortening in a collisional mountain belt. *Geological Society of America Special Paper,* 269, 1– 41. https://doi.org/10.1130/SPE269-p1

Cao, S. Y., Neubauer, F., Liu, J. L., Genser, J., & Leiss, B. (2011). Exhumation of the Diancang Shan metamorphic complex along the Ailao Shan-Red River belt, southwestern Yunnan, China: evidence from 40Ar/39Ar thermochronology. *Journal of Asian Earth Sciences,* 42, 525– 550. https://doi.org/10.1016/j.jseaes.2011.04.017

Carter, N. L., & Tsenn, M. C. (1987). Flow properties of continental lithosphere. *Tectonophysics,* 136, 27–63. https://doi.org/10.1016/0040-1951(87)90333-7

Chen, X. Y., Liu, J. L., Tang, Y., Song, Z. J., & Cao, S. Y. (2015). Contrasting exhumation histories along a crustal-scale strike-slip fault zone: The Eocene to Miocene Ailao Shan–Red River shear zone in southeastern Tibet. *Journal of Asian Earth Sciences,* 114, 174– 187. https://doi.org/10.1016/j.jseaes.2015.05.020

Chen, X. Y., Liu, J. L., Weng, S. T., Zou, Y. X., Kong, Y. L., Wu, W. B., Geng, X. L., Li, H. Y., & Zhang, S. H. (2016). Structural geometry and kinematic evolution of the Ailao Shan shear zone: Insights from integrated structural, microstructural and fabric studies of the Yaoshan complex, Yunnan, SW China. *International Geology Review,* 58, 849– 873.

Chen, X. Y., Liu, J. L., Qi, Y. C., Wang, K., Fan, W. K., Zhang, Y., & Chen, W. (2017). Miocene exhumation of the Ximeng dome in Yunnan, southeastern Tibet: Implication for intraplate deformation during extrusion of the Indochina block. *Journal of Asian Earth Sciences,* 141, 194– 212. https://doi.org/10.1080/00206814.2015.1136572

Chen, X. Y., Liu, J. L., Burg, J. P., Tang, Y., Wu, W. B., & Yan, J. X. (2020). Structural evolution and exhumation of the Yulong dome: Constraints on middle crustal flow in southeastern Tibetan Plateau in response to the India-Eurasia collision. *Journal of Structural Geology,* 137, 14170. https://doi.org/10.1016/j.jsg.2020.104070

Clark, M. K., & Royden, L. H. (2000). Topographic ooze: building the eastern margin of Tibet by lower crustal flow. *Geology,* 28, 703– 706. http://dx.doi.org/10.1130/0091-7613(2000)28<703:TOBTEM>2.0.CO;2

Clark, M. K., Bush, J. W. M., & Royden, L. H. (2005). Dynamic topography produced by lower crustal flow against rheological strength heterogeneities bordering the Tibetan Plateau. *Geophysical Journal International.,* 162, 575– 590. https://doi.org/10.1111/j.1365-246X.2005.02580.x

Davis, G. A., Lister, G. S., & Reynolds, S.J. (1986). Structural evolution of the Whipple and South Mountains shear zones, southwestern United States. *Geology,* 14(1), 7– 10. https://doi.org/10.1130/0091-7613(1986)14<7:SEOTWA>2.0.CO;2

Davis, G. A., Darby, B. J., Zheng, Y. D., & Spell, T. L. (2002). Geometric and temporal evolution of an extensional detachment fault, Hohhot metamorphic core complex, Inner Mongolia, China. *Geology,* 30, 1003– 1006. https://doi.org/10.1130/0091-7613(2002)030<1003:GATEOA>2.0.CO;2

Deng, J., Wang, Q. F., Li, G. J., Li, C. S., & Wang, C. M. (2014). Tethys tectonic evolution and its bearing on the distribution of important mineral deposits in the Sanjiang region, SW China. *Gondwana Research,* 26, 419– 437. https://doi.org/10.1016/j.gr.2013.08.002

Evans, M. A. (1994). Joints and décollement zones in Middle Devonian shales: Evidence for multiple deformation events in the central Appalachian Plateau. *Geological Society of America Bulletin,* 106(4), 447– 460. https://doi.org/10.1130/0016-7606(1994)106<0447:JADCZI>2.3.CO;2

Fountain, D. M., & Salisbury, M. H. (1981). Exposed cross-sections through the continental crust" implications for crustal structure, petrology, and evolution. *Earth and Planetary Science Letters,* 56, 263– 277.

https://doi.org/10.1016/0012-821X(81)90133-3

Gan, W. J., Zhang, P. Z., Shen, Z. K., Niu, Z. J., Wang, M., Wan, Y., Zhou, D. M., & Cheng, J. (2007). Present-day crustal motion within the Tibetan Plateau inferred from GPS measurements. *Journal of Geophysical Research: Solid Earth*, 112(B8). https://doi.org/10.1029/2005JB004120

Glover, P. W. J., & A. Ádám (2008), Correlation between crustal high conductivity zones and seismic activity and therole of carbon during shear deformation, *Journal of Geophysical Research: Solid Earth,* 113(B12). https://doi.org/10.1029/2008JB005804

Gilley, L. D., Harrison, T. M., Leloup, P. H., Ryerson, F. J., Lovera, O. M., & Wang, J. H. (2003). Direct dating of left-lateral deformation along the Red River shear zone, China and Vietnam. *Journal of Geophysical Research: Solid Earth,* 108 (B2), 2127. https://doi.org/10.1029/2001JB001726

Grasemann, B., Fritz, H., & Vannay, J. C. (1999). Quantitative kinematic flow analysis from the main central thrust zone (NW-Himalaya, India): implications for a decelerating strain path and the extrusion of orogenic wedges. *Journal of Structural Geology,* 21, 837– 853. https://doi.org/10.1016/S0191-8141(99)00077-2

Hansen, R. T. J., Bostock, M. G., & Christensen, N. I. (2012). Nature of the low velocity zone in Cascadia from receiver function waveform inversion. *Earth and Planetary Science Letters*, 337-338 (2012), 25– 38. https://doi.org/10.1016/j.epsl.2012.05.031

Harris, L. D., & Milici, R.C. (1977). Characteristics of thin-skinned style of deformation in the southern Appalachians and potential hydrocarbon traps. *U.S. Geological Survey Professional Paper,* 1018, 40. https://doi.org/10.3133/pp1018

Hoisch, T. D. (1989). A muscovite-biotite geothermometer. *American Mineralogist*, 74, 565– 572.

Ji, L., Liu, F. L., Wang, F., Cai, J., Wang, W., Tian, Z. H., & Liu, L. S. (2017). Ployphase metamorphism in Diancang Shan- Ailao Shan complex zone: Constraints from U- Pb dating and trace elements of zircons in metasedimenary

rocks, Gasa area. Acta Petrologica Sinica 33(2), 605－ 621 (in Chinese with English abstract).

Jolivet, L., Beyssac, O., Goffe, B., Avigad, D., Lepvrier, C., Maluski, H., & Thang, T. T. (2001). Oligo-miocene midcrustal subhorizontal shear zone in Indochina. Tectonics 20, 46– 57. https://doi.org/10.1029/2000TC900021

Kind, R., Ni, J., Zhao, W. J., Wu, J. X., Yuan, X. H., Zhao, L. S., Sandvol, E., Reese, C., Nabelek, J., & Hearn, T. (1996). Evidence from earthquake data for a partially molten crustal layer in Southern Tibet. *Science,* 274(5293), 1692– 1694. https://doi.org/10.1126/science.274.5293.1692

Lacassin, R., Schärer, U., Leloup, P. H., Arnaud, N., Tapponnier, P., Liu, X. H., & Zhang, L. S. (1996). Tertiary deformation and metamorphism SE of Tibet: the folded tiger-leap décollement of NW Yunnan, China. *Tectonics,* 15, 605– 622. https://doi.org/10.1029/95TC03749

Law, R. D., Searle, M. P., & Simpson, R. L. (2004). Strain, deformation temperatures and vorticity of flow at the top of the Greater Himalayan Slab, Everest Massif, Tibet. *Journal of the Geological Society, London,* 161, 305– 320.

Law, R. D., Stahr III, D. W., Francsis, M. K., Ashley, K. T., Grasemann, B., & Ahmad, T. (2013). Deformation temperatures and flow vorticities near the base of the Greater Himalayan Series, Sutlej Valley and Shimla Klippe, NW India. *Journal of Structural Geology,* 54, 21– 53. https://doi.org/10.1016/j.jsg.2013.05.009

Law, R. D. (2014). Deformation thermometry based on quartz c-axis fabrics and recrystallization microstructures: a review. *Journal of Structural Geology,* 66, 129– 161. https://doi.org/10.1016/j.jsg.2014.05.023

Leloup, P. H., & Kienast, J. R. (1993). High-temperature metamorphism in a major strike-slip shear zone: the Ailao Shan-Red River, People's Republic of China. *Earth and Planetary Science Letters,* 118, 213– 234. https://doi.org/10.1016/0012-821X(93)90169-A

Leloup, P. H., Lacassin, R., Tapponnier, P., Schärer, U., Zhong, D. L., Liu, X. H., Zhang, L. S., Ji, S. C., & Phan, T. T. (1995). The Ailao Shan-Red River shear zone (Yunnan, China), tertiary transform boundary of Indochina. *Tectonophysics,*

251, 3– 84. https://doi.org/10.1016/0040-1951(95)00070-4

Liu, J. L., Tang, Y., Tran, M. D., Cao, S. Y., Zhao, L., Zhang, Z. C., Zhao, Z. D., & Chen, W. (2012). The nature of the Ailao Shan–Red River (ASRR) shear zone: Constraints from structural, microstructural and fabric analysis of metamorphic rocks from Diancang Shan, Ailao Shan and Day Nui Con Voi high grade massifs. *Journal of Asian Earth Sciences,* 47, 231– 251. https://doi.org/10.1016/j.jseaes.2011.10.020

Liu, J. L., Chen, X. Y., Wu, W. B., Tang, Y., Tran, M. D., Nguyen, Q. L., Zhang, Z. C., & Zhao, Z. D. (2015). New tectono-geochronological constraints on timing of shearing along the Ailao Shan–Red River shear zone: Implications for genesis of Ailao Shan gold mineralization. *Journal of Asian Earth Science*, 103, 70– 86. https://doi.org/10.1016/j.jseaes.2014.11.006

Liu, J. L., Gan, H. N., Jiang, H., & Zhang, J. Y. (2017). Rheology of the middle crust under tectonic extension: Insights from the Jinzhou detachment fault zone of the Liaonan metamorphic core complex, eastern North China Craton. *Journal of Asian Earth Sciences,* 139, 61– 70. https://doi.org/10.1016/j.jseaes.2016.12.024

Liu, J. L., Chen, X. Y., Tang, Y., Song, Z. J., & Wang, W. (2020). The Ailao Shan-Red River shear zone revisited: timing and tectonic implications. *Geological Society of America Bulletin,* 132 (5-6), 1165– 1182. https://doi.org/ 10.1130/B35220.1

Liu, Z. C., Ji, J. Q., Sa, X., Chen, Y. P., & Zhong, D. L. (2018). Crustal deformation and tectonic levels of nujiang gorge since the miocene. *Science China Earth Sciences,* 61, 93– 108. https://doi.org/10.1007/s11430-017-9116-x

Mattauer, M. (1980). *Les déformations des matériaux de l'écorce terrestre,* pp., 124–131, Hermann, Paris.

McDonough, D T., & Fountain, D. M. (1988). Reflection characteristics of a mylonite zone based on compressional wave velocities of rock samples. *Geophysical Journal*, 93, 547– 558. https://doi.org/10.1111/j.1365-246X.1988.tb03880.x

Means, W. D., Hobbs, B. E., Lister, G. S., & Williams, P. F. (1980). Vorticity and non-coaxiality in progressive deformation. *Journal of Structural Geology*, 2, 371– 378. https://doi.org/10.1016/0191-8141(80)90024-3

Montomoli, C., Iaccarino, S., Carosi, R., Langone, A., & Visonà, D. (2013). Tectonometamorphic discontinuities within the Greater Himalayan Sequence in Western Nepal (Central Himalaya): insights on the exhumation of crystalline rocks. *Tectonophysics*, 608, 1349– 1370. https://doi.org/10.1016/j.tecto.2013.06.006

Montomoli, C., Carosi, R., & Iaccarino, S. (2015). Tectonometamorphic discontinuities in the Greater Himalayan Sequence: a local or a regional feature? In: Mukherjee, S., Carosi, R., van der Beek, P. A., Mukherjee, B.K., Robinson, D.M. (Eds.), Tectonics of the Himalaya. *Geological Society London Special Publications*, 412. 25– 41. https://doi.org/10.1144/SP412.3

Morley, C. K. (2002). A tectonic model for the Tertiary evolution of strike-slip faults and rift basins in SE Asia. *Tectonophysics*, 347, 189– 215. https://doi.org/10.1016/S0040-1951(02)00061-6

Nelson, K. D., Zhao, W., Brown, L. D., Kuo, J., Che, J., Lui, X., Klemper, S. L., Makovsky, Y., Meissner, R., Mechie, J., Kind, R., Wenzel, F., Ni, J., Nabelek, J., Leshou, C., Tan, H., Wei, W., Jones, A. G., Booker, J., Unsworth, M., Kidd, W. S. F., Hauck, M., Alsdorf, D., Ross, A., Cogan, M., Wu, C., Sandvol, E., & Edwards, M. (1996). Partially molten middle crust beneath southern Tibet: synthesis of Project INDEPTH initial results. *Science*, 274, 1684– 1688. https://doi.org/10.1126/science.274.5293.1684

Passchier, C. W. (1987). Stable positions of rigid objects in non-coaxial flow: a study in vorticity analysis. *Journal of Structural Geology*, 9, 679– 690. https://doi.org/10.1016/0191-8141(87)90152-0

Passchier, C. W., & R. A. J. Trouw (2005), *Microtectonics*, 2nd ed., 366 pp., Springer, Berlin.

Platt, J. P., Behr,W. M., & Cooper, F. J. (2015). Metamorphic core complexes: Windows into the mechanics and rheology of the crust. *Journal of the Geological Society*, 172(1), 9– 27. https://doi.org/10.1144/jgs2014-036

Ramsay, J. G. (1980). Shear zone geometry: a review. *Journal of Structural Geology*, 2, 83– 99. https://doi.org/10.1016/0191-8141(80)90038-3

Read, H. E., & Hegemier, G. A. (1984). Strain softening of rock, soil and concrete — a review article. *Mechanics of Materials,* 3, 271– 294. https://doi.org/10.1016/0167-6636(84)90028-0

Replumaz, A., Lacassin, R., Tapponnier, P., & Leloup, P. H. (2001). Large river odd sets and Pliocene-Quaternary dextral slip rate on the Red River fault (Yunnan, China). *Journal of Geophysical Research Atmospheres,* 106 (B1), 819– 836. https://doi.org/10.1029/2000JB900135

Rhodes, B. P., Blum, J., & Devine, T. (2000). Structural development of the mid-Tertiary Doi Suthep metamorphic complex and western Chiang Mai basin, northern Thailand. *Journal of Asian Earth Sciences,* 18, 97– 108. https://doi.org/10.1016/S1367-9120(99)00019-X

Ring, U., Bernet, M., & Tulloch, A. (2015). Kinematic, finite strain and vorticity analysis of the Sister Shear Zone, Steward Island, New Zealand. *Journal of Structural Geology,* 73, 114– 129. https://doi.org/10.1016/j.jsg.2015.02.004

Royden, L. H., Burchfiel, B. C., King, R. W., Wang, E., Chen, Z., Shen, F., & Liu, Y. (1997). Surface deformation and lower crustal flow in Eastern Tibet. *Science,* 276, 788– 790. https://doi.org/10.1126/science.276.5313.788

Schärer, U., Zhang, L. S., & Tapponnier, P. (1994). Duration of strike-slip movements in large shear zones: the Red River complex, China. *Earth and Planetary Science Letters,* 126, 379– 397. https://doi.org/10.1016/0012-821X(94)90119-8

Schoenbohm, L. M., Burchfiel, B. C., Chen, L. Z., & Yin, J. Y. (2006). Miocene to present activity along the Red River fault, China, in the context of continental extrusion, upper crustal rotation, and lower crustal flow. Geol. Soc. Am. Bull. 118, 672– 688. https://doi.org/10.1130/B25816.1

Scholz, C. H. (1988). The brittle-plastic transition and the depth of seismic faulting. *Geologische Rundschau,* 77, 319– 328. https://doi.org/10.1007/BF01848693

Searle, M. P., Law, R. D., Godin, L., Larson, K., Streule, M. J., Cottle, J. M., & Jessup, M. J. (2008). Defining the Himalayan Main Central Thrust in Nepal. *Journal of the Geological Society,* 165, 523– 534. https://doi.org/10.1144/0016-76492007-081

Searle, M. P., Yeh, M. W., Lin, T. H., & Chung, S. L. (2010). Structural constraints on the timing of left-lateral shear along the Red River shear zone in the Ailao Shan and Diancang Shan Ranges, Yunnan, SW China. *Geosphere,* 6, 316– 338. https://doi.org/10.1130/GES00580.1

Simpson, C., & De Paor, D. G. (1993). Strain and kinematic analysis in general shear zones. *Journal of Structural Geology,* 15, 1– 20. https://doi.org/10.1016/0191-8141(93)90075-L

Simpson, C., Whitmeyer, S. J., de Paor, D. G., Gromet, L. P., Miro, R., Krol, M. A., & Short, H. (2001). Sequential ductile to brittle reactivation of major fault zones along the accretionary margin of Gondwana in Central Argentina, in R. E. Holdsworth, R. A. Strachan (Eds), The Nature and Tectonic Significance of Fault Zone Weakening, *Geological Society London Special Publications*, 186(1):233-255. https://doi.org/10.1144/GSL.SP.2001.186.01.14

Stipp, M., Stünitz, H., Heilbronner, R., & Schimid, S. M. (2002). The eastern Tonale fault zone: A“natural laboratory” for crystal plastic deformation of quartz over a temperature range from 250 to 700 °C. *Journal of Structural Geology*, 24, 1861–1884. https://doi.org/10.1016/S0191-8141(02)00035-4

Sun, A. H., & Zhao, D. P. (2020). Anisotropic Tomography Beneath Northeast Tibet: Evidence for Regional Crustal Flow. *Tectonics*, 39, e2020TC006161. https://doi.org/10.1029/2020TC006161

Tang, Y., Liu, J. L., Tran, M. D., Song, Z. J., Wu, W. B., Zhang, Z. C., Zhao, Z. D., & Chen, W. (2013). Timing of left-lateral shearing along the Ailao Shan–Red River shear zone: Constraints from zircon U-Pb ages from granitic rocks in the shear zone along the Ailao Shan Range, western Yunnan, China. *International Journal of Earth Sciences*, 102, 605– 626. https://doi.org/10.1007/s00531-012-0831-y

Tapponnier, P., & Molnar, P. (1976). Slip-line field theory and large-scale continental tectonics. *Nature,* 264 (5584), 319– 324. https://doi.org/10.1038/264319a0

Tapponnier, P., Peltzer, G., Le Dain, A. Y., Armijo, R., & Cobbold, P. (1982). Propagating extrusion tectonics in Asia: new insights from simple experiments with plasticine. *Geology,* 10 (12), 611– 616.

https://doi.org/10.1130/0091-7613(1982)10<611:PETIAN>2.0.CO;2

Tapponnier, P., Lacassin, R., Leloup, P. H., Schärer, U., Zhong, D. L., Liu, X. H., Ji, S. C., Zhang, L. S., & Zhong, J. (1990). The Ailao Shan-Red River metamorphic belt: tertiary left lateral shear between Sundaland and South China. *Nature*, 343, 431– 437. https://doi.org/10.1038/343431a0

Tapponnier, P., Xu, Z. Q., Roger, F., Meyer, B., Arnaud, N., Wittlinger, G., & Yang, J. S. (2001). Oblique stepwise rise and growth of the Tibet Plateau. *Science*, 294 (5547), 1671– 1677. https://doi.org/10.1126/science.105978

Thomas W. A. (1990). Controls on locations of transverse zones in thrust belts. *Eclogae Geologicae Helvetiae*, 83, 727– 744.

Tikoff, B., & Teyssier, C. (1994). Strain and fabric analyses based on porphyroclast interaction. *Journal of Structural Geology*, 16, 477– 491. https://doi.org/10.1016/0191-8141(94)90092-2

Tikoff, B., & Fossen, H. (1995). The limitations of three-dimensional kinematic vorticity analysis. *Journal of Structural Geology*, 17, 1771– 1784. https://doi.org/10.1016/0191-8141(95)00069-P

Tran, N. N., Mitsuhiro, T., & Tetsumaru, I. (1998). P–T–t paths and post-metamorphic exhumation of the Day Nui Con Voi shear zone in Vietnam. *Tectonophysics*, 290, 299–318. https://doi.org/10.1016/S0040-1951(98)00054-7

Trouw, R. A. J., Passchier, C. W., & Wiersma, D. (2010). *Atlas of Mylonites and related Microstructures.* Pp., Springer-Verlag, Berlin, Heidelberg. https://doi.org/10.1007/978-3-642-03608-8

Wagner, T., Lee, J., Hacker, B. R., & Seward, G. (2010). Kinematics and vorticity in Kangmar Dome, southern Tibet: Testing midcrustal channel flow models for the Himalaya. *Tectonics*, 29(6), TC6011. https://doi.org/10.1029/2010TC002746

Wang, P. L., Lan., C. Y., Yem, N. T., Lo, C. H., Lee, T. Y., & Chung, S. L. (1998). Thermochronological evidence for the movement of the Ailao Shan–Red River shear zone: a perspective from Vietnam. *Geology*, 26, 887– 890. https://doi.org/10.1130/0091-7613(1998)026<0887:TEFTMO>2.3.CO;2

Wang, Q., Zhang, P. Z., Freymueller, J. T., Bilham, R., Larson, K. M., Lai, X., You, X.,

Niu, Z., Wu, J., Li, Y., Liu, J., Yang, Z., & Chen, Q. (2001). Present-day crustal deformation in China constrained by Global Positioning System measurements. *Science*, 294, 574– 577. https://doi.org/10.1126/science.1063647

Wang, Q. F., Deng, J., Li, C. S., Li, G. J., Yu, L., & Qiao, L. (2014). The boundary between the Simao and Yangtze blocks and their locations in Gondwana and Rodinia: constraints from detrital and inherited zircons. *Gondwana Research,* 26, 438– 448. https://doi.org/10.1016/j.gr.2013.10.002

Wang, Y. J., Fan, W. M., Zhang, Y. H., Peng, T. P., Chen, X. Y., & Xu, Y. G. (2006). Kinematics and 40Ar/39Ar geochronology of the Gaoligong and Chongshan shear systems, western Yunnan, China: Implications for early Oligocene tectonic extrusion of SE Asia. *Tectonophysics,* 418, 235– 254. https://doi.org/10.1016/j.tecto.2006.02.005

Wallis, S. R. (1992). Vorticity analysis in a metachert from the Sanbagawa belt, SW Japan. *Journal of Structural Geology,* 14, 271– 280. https://doi.org/10.1016/0191-8141(92)90085-B

Wallis, S. R., Platt, J. P., & Knott, S. D. (1993). Recognition of syn-convergence extension in accretionary wedges with examples from the Calabrian arc and the eastern Alps. *American Journal of Science,* 293, 463– 495. https://doi.org/10.2475/ajs.293.5.463

Wallis, S. R. (1995). Vorticity analysis and recognition of ductile extension in the Sanbagawa belt, SW Japan. *Journal of Structural Geology,* 17, 1077– 1093. https://doi.org/10.1016/0191-8141(95)00005-X

Wei, W. B., Unsworth, M., Jones, A., Booker, J., Tan, H. D., Nelson, D., Chen, L., Li, S., Solon, K., Bedrosian, P., Jin, S., Deng, M., Ledo, J., Kay, D., & Roberts, B. (2001). Detection of Widespread Fluids in the Tibetan Crust by Magnetotelluric Studies. *Science,* 292, 716– 718. https://doi.org/10.1126/science.1010580

Wintsch, R. P., & Yeh, M. W. (2013). Oscillating brittle and viscous behavior through the earthquake cycle in the red river shear zone: Monitoring flips between reaction and textural softening and hardening. *Tectonophysics*, 587, 46– 62. https://doi.org/10.1016/j.tecto.2012.09.019

Wu, C. M., & Chen, H. X. (2015a). Revised Ti-in-biotite geothermometer for ilmeniteor rutile-bearing crustal metapelites. *Science Bulletin*, 60(1), 116– 121. https://doi.org/10.1007/s11434-014-0674-y

Wu, C. M., & Chen, H. X. (2015b). Calibration of a Ti-in-muscovite geothermometer for ilmenite–and Al_2SiO_5-bearing metapelites. *Lithos*, 212-215, 122–127. https://doi.org/10.1016/j.lithos.2014.11.008

Wu, W. B., Liu, J. L., Chen, X. Y., & Zhang, L. S. (2016). Zircon U-Pb geochronology, Hf isotopic characteristics and tectonic implications of the Early-Middle Triassic granitoids in the high-grade metamorphic belt of Ailaoshan, southeastern Tibet. *International Journal of Earth Sciences*, 106, 875– 897. https://doi.org/10.1007/s00531-016-1339-7

Wu, W. B., Liu, J. L., Zhang, L. S., Qi, Y. C., & Ling, C. Y. (2017). Characterizing a middle to upper crustal shear zone: Microstructural, quartz c-axis fabric, deformation temperature and flow vorticity analysis of the northern Ailao Shan–Red River shear zone. *Journal of Asian Earth Sciences*, 139, 95–114. https://doi.org/10.1016/j.jseaes.2016.12.026

Xypolias, P., Spanos, D., Chatzaras, V., Kokkalas, S., & Koukouvelas, I. (2010). Vorticity of flow in ductile thrust zones: examples from the Attico-Cycladic Massif (Internal Hellenides, Greece). In R. D. Law, R. W. H. Butler, R. E. Holdsworth, M. Krabbendam, R. A. Strachan (Eds.), Continental Tectonics and Mountain Building: The Legacy of Peach and Horne, Special Publications (Vol. 335, pp. 687– 714). London: Geological Society.

Xu, T. Y., Ji, J. Q., Tu, J. Y., & Liu, Z. C. (2012). Tectonic levels and deformation patterns of the eastern Sichuan fold belt. *Chinese Journal of Geology*, 47, 788–807 (in Chinses with English abstract).

Xu, Z. Q., Wang, Q., Cai, Z. H., Dong, H. W., Li, H. Q., Chen, X. J., Duan, X. D., Cao, H., Li, J., & Burg, J. P. (2015). Kinematics of the Tengchong Terrane in SE Tibet from the late Eocene to early Miocene: insights from coeval mid-crustal detachments and strike-slip shear zones. Tectonophysics, 665, 127– 148. https://doi.org/10.1016/j.tecto.2015.09.033

Yan J. X., Zhang, T. Y., Liu, J. L., Chen, X. Y., Chen, W., Dao, H. M. (2021). Lateral subhorizontal middle to lower crustal flow in response to continental collision: Evidence from the Diancang Shan complex along the Ailao Shan-Red River belt, Southeastern Tibetan Plateau. *Journal of Structural Geology,* 143, 104234. https://doi.org/10.1016/j.jsg.2020.104234

Yang, Y., Ritzwoller, M. H., Zheng, Y., Shen, W. S., Levshin, A. L., & Xie, Z. (2012). A synoptic view of the distribution and connectivity of the mid-crustal low velocity zone beneath Tibet. *Journal of Geophysical Research: Solid Earth,* 117, B04303. https://doi.org/10.1029/2011JB008810

Yeh, M. W., Lee, T. Y., Lo, C. H., Chung, S. L., Lan, C. Y., & Anh, T. T. (2008). Structural evolution of the Day Nui Con Voi metamorphic complex: implications on the development of the Red River Shear Zone, Northern Vietnam. *Journal of Structural Geology,* 30, 1540– 1553. https://doi.org/10.1016/j.jsg.2008.08.007

Yin, A., & Dunn, J. F. (1992). Structural and stratigraphic development of the Whipple–Chemehuevi detachment fault system, southeastern California: Implications for the geometrical evolution of domal and basinal low–angle normal faults. *Geological Society of America Bulletin,* 104(6), 659– 674. https://doi.org/10.1130/0016-7606(1992)104<0659:SASDOT>2.3.CO;2

Yoshino, T., & Noritake, F. (2011). Unstable graphite films on grain boundaries in crustal rocks. *Earth and Planetary Science Letters*, 306 (3-4), 186– 192. https://doi.org/10.1016/j.epsl.2011.04.003.

Zhong, D. L. (1998). *The Paleo-Tethyan Orogenic Belts, Western Yunnan and Sichuan Provinces (in Chinese)*. Science Press, Beijing.

Zhang, B., Yin, C. Y., Zhang, J. J., Wang, J. M., Zhong, D. L., Wang, Y., Lai, Q. Z., Yue, Y. H., & Zhou, Q. Y. (2017a). Midcrustal shearing and doming in a Cenozoic compressive setting along the Ailao Shan-Red River shear zone. *Geochemistry Geophysics Geosystems,* 18, 400– 433. https://doi.org/10.1002/2016GC006520.

Zhang, B., Chai, Z., Yin, C. Y., Huang, W. T., Wang, Y., Zhang, J. J., Wang, X. X., & Cao, K. (2017b). Intra-continental transpression and gneiss doming in an

obliquely convergent regime in SE Asia. *Journal of Structural Geology,* 97, 48–70. https://doi.org/10.1016/j.jsg.2017.02.010

Zhang, J. J., Zhong, D. L., Sang, H. Q., & Zhou. Y. (2006). Structural and geochronological evidence for multiple episodes of deformation along the ailao shan-red river shear zone, Southeastern Asia, since paleocene. *Acta Geologica Sinica (English Edition),* 80(1), 79- 96. https://doi.org/10.1111/j.1755-6724.2006.tb00798.x

Zhang, P. Z., Shen, Z. K., Wang, M., Gan, W. J., Burgmann, R., Molnar, P., Wang, Q., Niu, Z. J., Sun, J. Z., Wu, J. C., Sun, H. R., & You, X. Z. (2004). Continuous deformation of the Tibetan Plateau from Global positioning system data. *Geology,* 32, 809– 812. https://doi.org/10.1130/G20554.1

Zheng, Y. Y., Liu. J. L., Hou, C. R., Sun, Y. Q., & Craddock, J. P. (2021). Exhumation of metamorphic core complexes through progressive subhorizontal shearing, doming and detachment faulting: insights from the Cretaceous Liaonan metamorphic core complex, eastern North China craton. *Lithosphere*, https://doi.org/10.1002/essoar.10501998.1

Zhou, M. F., Yan, D. P., Kennedy, A. K., Li, Y., & Ding, J. (2002). SHRIMP U–Pb zircon geochronological and geochemical evidence for Neoproterozoic, arc-magmatism along the western margin of the Yangtze block, South China. *Earth and Planetary Science Letters,* 196, 51– 67. https://doi.org/10.1016/S0012-821X(01)00595-7

Appendix

Appendix A. Mineral element composition and deformation temperature estimate results.

Appendix B. Homogenisation temperature and salinity of quartz vein fluid inclusions.